

Water Resources Research

RESEARCH ARTICLE

10.1029/2018WR024446

Key Points:

- A weather-regime stochastic weather generator is presented to support process-informed climate vulnerability assessments of water systems
- Climate change perturbations can be specified separately for thermodynamic and dynamical processes
- The model is developed to be broadly applicable across the western United States in the cold season

Supporting Information:

- Supporting Information S1

Correspondence to:

S. Steinschneider,
ss3378@cornell.edu

Citation:

Steinschneider, S., Ray, P., Rahat, S. H., & Kucharski, J. (2019). A weather-regime-based stochastic weather generator for climate vulnerability assessments of water systems in the western United States. *Water Resources Research*, 55, 6923–6945. <https://doi.org/10.1029/2018WR024446>

Received 18 NOV 2018

Accepted 22 JUL 2019

Accepted article online 30 JUL 2019

Published online 19 AUG 2019

A Weather-Regime-Based Stochastic Weather Generator for Climate Vulnerability Assessments of Water Systems in the Western United States

Scott Steinschneider¹ , Patrick Ray² , Saiful Haque Rahat², and John Kucharski³

¹Department of Biological and Environmental Engineering, Cornell University, Ithaca, NY, USA, ²Department of Chemical and Environmental Engineering, University of Cincinnati, Cincinnati, OH, USA, ³Institute for Water Resources, Hydrologic Engineering Center, Davis, CA, USA

Abstract Vulnerability-based frameworks are increasingly used to better understand water system performance under climate change. This work advances the use of stochastic weather generators for climate vulnerability assessments that simulate weather based on patterns of regional atmospheric flow (i.e., weather regimes) conditioned on global-scale climate features. The model is semiparametric by design and includes (1) a nonhomogeneous Markov chain for weather regime simulation; (2) block bootstrapping and a Gaussian copula for multivariate, multisite weather simulation; and (3) modules to impose thermodynamic and dynamical climate change, including Clausius-Clapeyron precipitation scaling, elevation-dependent warming, and shifting dynamics of the El Niño–Southern Oscillation (ENSO). In this way, the model can be used to evaluate climate impacts on water systems based on hypotheses of dynamic and thermodynamic climate change. The model is developed and tested for cold-season climate in the Tuolumne River Basin in California but is broadly applicable across the western United States. Results show that eight weather regimes exert strong influences over local climate in the Tuolumne Basin. Model simulations adequately preserve many of the historical statistics for precipitation and temperature across sites, including the mean, variance, skew, and extreme values. Annual precipitation and temperature are somewhat underdispersed, and precipitation spell statistics are negatively biased by 1–2 days. For simulations of future climate, the model can generate a range of Clausius-Clapeyron scaling relationships and modes of elevation-dependent warming. Model simulations also suggest a muted response of Tuolumne climate to changes in ENSO variability.

1. Introduction

Climate change poses a major threat to the sustainability of water systems. To better understand this threat, planners require future climate scenarios that are used to test the robustness of their system to different components of climate change. However, how these scenarios can be generated in an internally consistent and computationally efficient manner for risk-based water system studies remains an open question.

General circulation models (GCMs) of the ocean and atmosphere are a valuable tool for describing how physical processes in the climate system drive predictability and variability in local weather. Projections from these numerical models over multidecadal timescales (Taylor et al., 2012) provide internally consistency scenarios that can be used to examine the impacts of anthropogenic climate change on water system performance (Brekke et al., 2009; Jiménez Cisneros et al., 2014). These impacts are often linked to changes in climate thermodynamics and the intensification of the water cycle, including greater evapotranspiration and enhanced droughts (Dai, 2011; Trenberth et al., 2014) and more intense precipitation resulting from increases in the moisture carrying capacity of a warmer atmosphere (i.e., the Clausius-Clapeyron [CC] relationship; Trenberth, 2011).

However, there are well-acknowledged deficiencies in GCM-based representations of regional climate, particularly for precipitation and the atmospheric water cycle (Kysely et al., 2015; Stephens et al., 2010; Tan et al., 2018), and this complicates their use in long-term impact assessments (Fowler et al., 2007). Higher-resolution models can improve some aspects of modeled climate (Kendon et al., 2017), but they necessarily reduce computational efficiency. This can limit ensemble simulations needed for risk-based assessments of critical water infrastructure. Changes in atmospheric dynamics (i.e., the organization and

persistence characteristics of atmospheric circulation) can also play a critical role in regional climate change (Lu et al., 2014; O’Gorman, 2015). However, these changes are highly uncertain under future emissions scenarios (Shepherd, 2014). Improved model resolution does not necessarily improve precipitation biases linked to atmospheric dynamics (Maher et al., 2018; Muñoz et al., 2017). Furthermore, statistical corrections to these dynamical biases are not straightforward, since they are linked to modeled physical processes that could change under global warming (Stephenson et al., 2012).

Stochastic weather generators provide a computationally efficient complement to GCMs for investigating water system performance under climate stress. These models are parameterized based on existing meteorological records and are then used to generate large ensembles of simulated daily weather records that are similar to but not bound by variability in past observations (Fowler et al., 2007; Richardson, 1981; Wilks & Wilby, 1999). For water system applications, weather generators must often develop sequences of multiple weather variables (e.g. precipitation, temperature, and wind speed) at multiple locations while maintaining realistic persistence and covariance structures associated with transient, multiday storm events and over longer (seasonal-interannual) timescales. Parametric (e.g., latent Gaussian processes, copulas, and wavelet-based time series simulation) and nonparametric (e.g., bootstrapping, Schaake Shuffle) approaches to preserve the complex space-time characteristics of weather variability remain at the forefront of research in the field (Allard & Bourotte, 2015; Breinl et al., 2017; Evin et al., 2018; Kwon et al., 2009; Li & Babovic, 2018; Sparks et al., 2018; Steinschneider & Brown, 2013; Verdin et al., 2018). However, hybrid models that use both parametric and nonparametric modules have proven well suited for generating multisite, multivariate climate sequences that differ from those in the historical record without undue model complexity (Apipattanavis et al., 2007; Sparks et al., 2018; Steinschneider & Brown, 2013).

Once fit to historical data, model parameters can be systematically altered to produce new traces of weather that exhibit a wide range of change in their distributional characteristics, including the intensity and frequency of average and extreme precipitation and the recurrence and depth of multi-year droughts. This approach has often been used to downscale seasonal forecasts or decadal projections from GCMs to the local scale (Wilks, 2002, 2010, 2012). More recently, it has been adopted in a vulnerability-based or “bottom-up” framework to test water system performance under a range of climate scenarios that extend beyond those projected by climate model ensembles (Singh et al., 2014; Steinschneider, McCrary, Mearns, & Brown, 2015; Steinschneider, McCrary, Wi, et al., 2015; Steinschneider, Wi, & Brown, 2015; Yates et al., 2015; Quinn et al., 2018; Guo et al., 2018). This latter approach enables a thorough exploration of system sensitivities to small perturbations in the underlying climate that might not be captured when using a relatively small and often biased GCM ensemble.

To date, the use of stochastic weather generators in bottom-up climate vulnerability assessments has largely been confined to exploratory analyses that test the sensitivity of water infrastructure to changes in summary statistics of weather variables (e.g., the mean, variance, seasonality, intermittency, or frequency and magnitude of extreme precipitation). Notably, an explicit link to thermodynamic and dynamic pathways in the climate system that control these features is missing. Therefore, the results of these analyses often highlight potential vulnerabilities of water systems to nuanced climate change but cannot provide a clear indication of whether those climate scenarios are physical plausible, let alone likely to occur in the future (Knighton et al., 2017). Consequently, the impact analysis remains unconstrained, with important implications: system adaptations designed to be robust to implausible scenarios may be too conservative and prone to costly over-design, but those that ignore plausible scenarios could lack the capacity to adapt to future change.

There is a need for process-informed stochastic models that create a formalized link between causal pathways in the climate system, local weather scenarios, and water system vulnerabilities. This would advance climate scenario development by allowing projections of global and regional scale climate processes, which are most credibly simulated by GCMs (Farnham et al., 2018; Johnson & Sharma, 2009), to constrain scenario development and system vulnerability discovery. Weather-regime-based stochastic weather generators, like the one presented in this paper, are a promising tool for this purpose.

Weather regimes (WRs) are recurring large-scale atmospheric flow patterns (e.g., upper-level, quasi-stationary blocks and troughs) that appear at fixed geographic locations, persist for days-to-weeks within a season, and organize high-frequency weather systems (Robertson et al., 2015; Robertson & Ghil, 1999).

They represent intermediary phenomena in the stochastic continuum of atmospheric perturbations that connect local weather to hemispheric circulation. WR-based stochastic weather generators are hierarchical models that utilize WRs as an organizing principal for stochastic simulation (Ailliot et al., 2015). WRs are identified directly through machine-learning on large-scale circulation fields (Conticello et al., 2018; Muñoz et al., 2017; Robertson et al., 2015) or as latent processes (i.e., Hidden Markov Models) associated with regional patterns of surface climate (Holsclaw et al., 2016; Hughes & Guttorp, 1994; Robertson et al., 2004). They can be modeled effectively as a Markovian process. The simulation of daily weather is then conditioned on the modeled WRs, while transitions between WRs are conditioned on boundary forced, large-scale teleconnection patterns like the El Niño–Southern Oscillation (ENSO).

WR-based stochastic weather generators can be used to translate emerging hypotheses of decadal-scale changes in climate dynamics and thermodynamics into water system impacts. A variety of changes to large-scale climate drivers can be parameterized and propagated into the frequency of simulated WRs and associated surface climate fields, thereby generating scenarios of dynamical change. Examples of these dynamical changes include increased meridional fluctuations in the jet stream (Francis & Vavrus, 2015), intensification of Northern Hemisphere subtropical highs (Li et al., 2012), changing frequency of ENSO events (Cai et al., 2014, 2015), and shifting ENSO teleconnections to surface climate (Yeh et al., 2018).

Hypothesized thermodynamic change can also be tested by adjusting the distribution of local temperature and precipitation directly, regardless of WR. These changes include seasonal (Cai & Tung, 2012; Rangwala, 2013; Sejas et al., 2014) and elevation-dependent (Pepin et al., 2015; Rangwala et al., 2016) warming, which are critical aspects of temperature change for snow accumulation and melt processes in mountainous regions (e.g., the western United States). They also include the magnitudes of extreme precipitation events, which are expected to increase at least as fast as the increase in atmospheric moisture holding capacity ($\sim 7\% \text{ C}^{-1}$, $1\times \text{CC}$ -scaling; Trenberth, 2011; Fischer & Knutti, 2016), but could increase faster due to latent heat release during intense precipitation that further enhances convection and precipitation rates (Bao et al., 2017; Guerreiro et al., 2018; Lenderink et al., 2017; Westra et al., 2014). The separate consideration of thermodynamic and dynamic mechanisms of climate change can help focus and constrain the generation of stochastic climate scenarios for vulnerability assessments to ensure their physical plausibility.

This study contributes a WR-based stochastic weather generator for climate vulnerability assessments of water systems in the western United States. The generator is tailored for the climate of this region in the cold season, which is dominated by synoptic-scale storm systems governed by midlatitude atmospheric dynamics. The model is semiparametric by design and includes (1) a nonhomogeneous Markov chain for WR simulation; (2) block bootstrapping and a Gaussian copula for multivariate, multisite weather simulation; and (3) modules to impose thermodynamic and dynamical climate change, including CC precipitation scaling, elevation dependent warming, and shifting ENSO dynamics. To our knowledge, this is the first stochastic weather generator developed for vulnerability assessments that makes explicit linkages between dynamic and thermodynamic climate change pathways and local weather. For demonstrative purposes we fit and test the model in the Tuolumne River Basin in California, a tributary of the San Joaquin River. However, the model is broadly applicable across the western United States.

2. Study Region and Data

The proposed weather generator utilizes information on large-scale atmospheric flow over the Pacific/North American sector to define WRs and develop conditional simulations of local weather systems over the western United States. To quantify atmospheric flow, daily 500-hPa geopotential heights were taken from the National Centers for Environmental Prediction/Department of Energy Reanalysis 2 dataset ($2.5^\circ \times 2.5^\circ$ resolution; Kanamitsu et al., 2002) over the cold season (November–March) between water years (WY) 1980–2017, where WYs are defined from 1 October through 30 September. During the cold season, these data are reflective of the position and orientation of upper level troughs and ridges that direct storm tracks over the continent (Milrad, 2018).

To better understand the predominant weather systems occurring during each WR, we also calculate daily zonal and meridional vertically integrated water vapor transport (IVT) from 1,000 to 300 hPa using the same reanalysis product:

$$IVT_u = \int_{1,000}^{300} \frac{uq}{g} dp \quad (1)$$

$$IVT_v = \int_{1,000}^{300} \frac{vq}{g} dp \quad (2)$$

where u and v are daily zonal and meridional wind speeds, q is daily specific humidity, p is pressure level, and g is the standard acceleration of gravity (9.8 m/s^2). In addition, we collect occurrences of atmospheric river (AR) landfalls along the western U.S. coast from the recent dataset of Brands et al. (2017). This dataset identifies AR landfalls across broad regions of western North America based on IVT from four different reanalysis datasets (we use the ERA-interim product; Dee et al., 2011) and different combinations of AR detection and tracking thresholds. We aggregate this daily data to calculate the number of landfalling ARs impacting southern California (south of 38°N) and Northern California/Pacific Northwest (north of 38°N) for each cold-season between WYs 1980 and 2014.

The weather generator is demonstrated for the Tuolumne River Basin, a tributary of the San Joaquin River and a major source for the San Francisco regional water system (Figure 1). The Tuolumne watershed originates in Yosemite National Park and includes a sharp elevation gradient in the headwaters from less than 1,000 m above sea level (m asl) to approximately 4,000 m asl in approximately 30 km. Daily precipitation, maximum temperature, and minimum temperature are collected across the Tuolumne Basin from the gridded meteorological dataset of Livneh et al. (2015). These data are provided at a $1/16^\circ$ resolution, with 160 gridded locations inside the Tuolumne Basin between 37.4°N – 38.3°N and 239.2°E – 240.9°E , and are interpolated from gage data and topographically scaled using the SYMAP (Shepard, 1984) and PRISM (Daly et al., 1994) algorithms, respectively. We also collect historical ground-level observations from the National Centers for Environmental Information Global Historical Climatology Network for five meteorological stations within and around the Tuolumne basin: Sonora (510 m asl), Groveland (950 m asl), Hetch Hetchy (1,180 m asl), Yosemite (1,220 m asl), and Gaylor (2,825 m asl).

Finally, a monthly Niño 3.4 index is taken from the National Oceanic and Atmospheric Administration (NOAA) Climate Prediction Center based on the NOAA Extended Reconstructed Sea Surface Temperature (ERSST) v5 sea surface temperature dataset (Huang et al., 2017). A seasonal index is created by averaging monthly anomalies between December–February (DJF) for WYs 1949–2017.

3. The Weather Generator

The proposed weather generator is a semiparametric model akin to those in Apipattanas et al. (2007) and Steinschneider and Brown (2013) with a hierarchical structure composed of three primary modules: (1) identification and simulation of WRs that dictate the large-scale atmospheric flow across the entire western United States, (2) simulation of local weather conditioned on the WRs, and (3) perturbations to the simulation schemes in (1) and (2) reflective of dynamical and thermodynamic climate change, respectively. An overview of the approach is presented in Figure 2.

3.1. WR Module

3.1.1. Identification of Regimes

Following Robertson and Ghil (1999), patterns of daily, large-scale circulation over the Pacific/North American sector for each day in the record are characterized using K -means clustering on standardized 500-hPa height anomalies between 30°N – 60°N and 180°E – 260°E . To reduce the dimensionality of the clustering problem, heights are first projected onto their first J empirical orthogonal functions (EOFs), where J is chosen using a scree test and also to ensure that the selected EOFs explain a large (e.g., $>80\%$) degree of the variance in the data. K -means clustering is then conducted on the first J principal components (PCs) and used to partition each day in the record into one of K separate states, or WRs. The result is a vector, WR , with values from 1 to K (i.e., one of the WRs) for each day of the instrumental record. The number K of WRs is selected using a scree test, such that additional WRs explain increasingly marginal amounts of variability of the J PCs. All daily data from the entire cold season and all years of record are used in this clustering procedure, so that no distinctions are made between WRs across months. To ensure that circulation anomalies within a cluster are relatively homogenous, we repeat the above procedure for all days classified into each of the K WRs and examine composites of circulation for the subclusters. If large-scale circulation anomalies

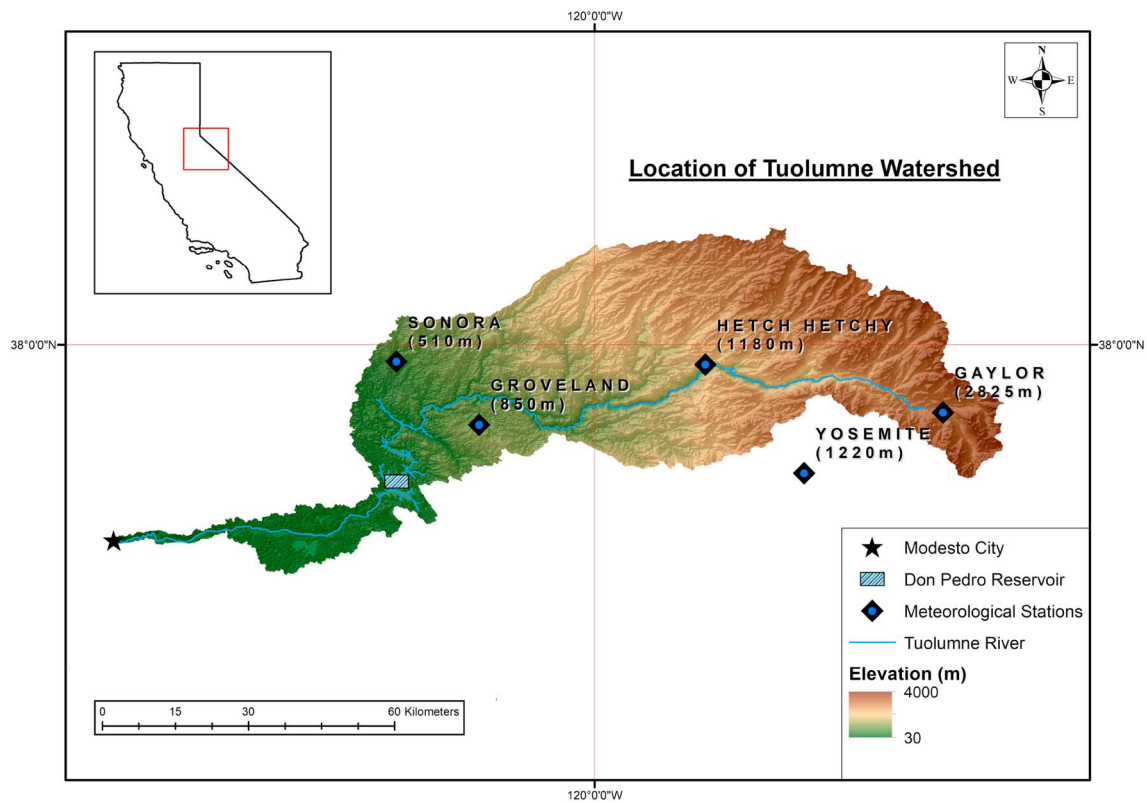


Figure 1. Map of the Tuolumne watershed.

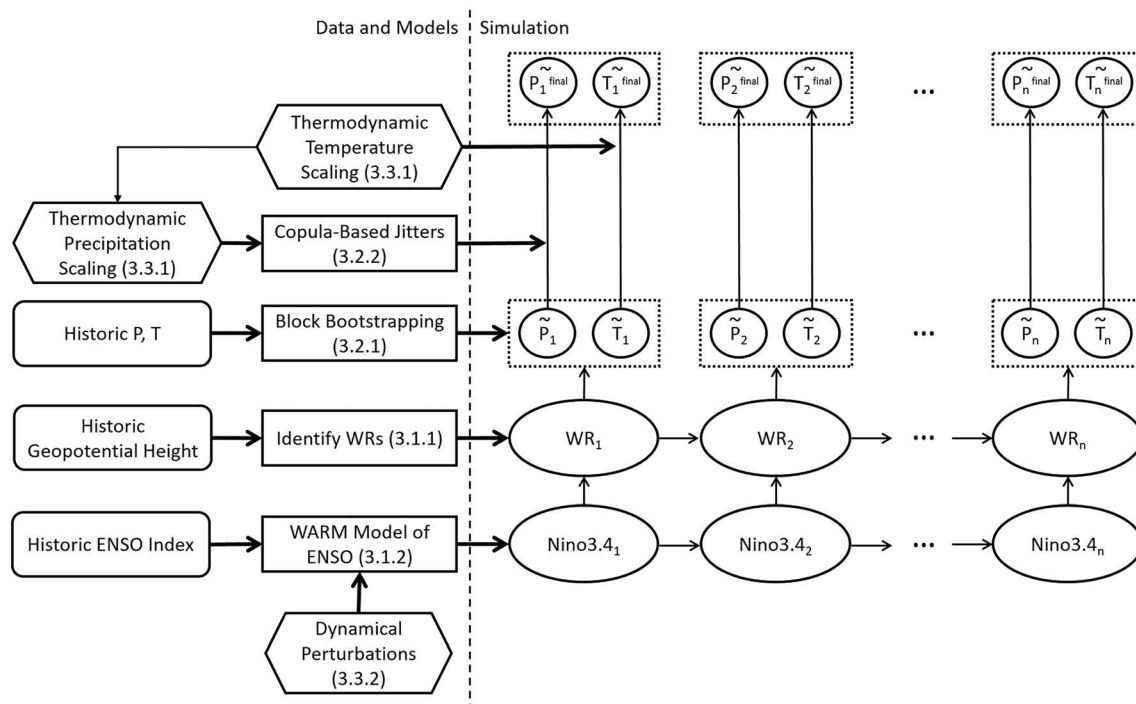


Figure 2. Flowchart of the overall approach.

across subclusters for a particular WR are sufficiently different, we repeat the original clustering but with $K+1$ WRs and iterate this process until circulation is relatively homogenous across sub-clusters of each WR.

3.1.2. Nonhomogenous Markov Model

The states are modeled as a first-order Markov chain, after confirming this choice with a χ^2 test (Anderson & Goodman, 1957). The probability $P(WR_t = i | WR_{t-1} = j)$ of WR j transitioning to WR i is embedded in a $K \times K$ transition probability matrix, which is assumed nonhomogeneous in time. The state transitions are modeled using a multinomial logistic regression:

$$P(WR_t = i | WR_{t-1} = j, \mathbf{X}_t = \mathbf{x}) = \frac{\exp(\beta_{0j,i} + \beta_{ji}' \mathbf{x})}{\sum_{k=1}^K \exp(\beta_{0j,k} + \beta_{jk}' \mathbf{x})} \quad (3)$$

where \mathbf{X}_t is a vector of daily covariates for day t , $\beta_{0j,i}$ is an intercept, β_{ji} is a vector of regression parameters, and a prime denotes the vector transpose. If \mathbf{X}_t is set to a null vector, then the estimation of equation (3) for each conditioning state j reproduces a homogeneous transition probability matrix for the vector WR. In this study, we set $\mathbf{X}_t' = [\text{Nino3.4}_t, \text{Month}_t]$ a vector containing the DJF average value of the Niño 3.4 index repeated for each day t of the given cold season and the calendar month for day t . This leads to a transition probability matrix that varies in each month and year of the simulation and captures the seasonal cycle of WRs and the teleconnection between WR frequencies and ENSO.

To enable simulations beyond historical ENSO variability, the DJF Niño 3.4 index is modeled using a wavelet autoregressive model (WARM; Kwon et al., 2007). The WARM model uses wavelets to decompose the Niño 3.4 index into H orthogonal component series that represent low-frequency signals and a noise component:

$$\text{Nino3.4}_t = \sum_{h=1}^H Z_{h,t} + \varepsilon_t \quad (4)$$

The decomposed times series $Z_{h,t}$ and noise ε_t are then stochastically simulated using autoregressive moving average models, and then summed together to synthesize a simulated Niño 3.4 index. A small variance correction factor is applied to the final simulated index, following Nowak et al. (2011). By simulating each signal separately, the WARM model can better reproduce spectral signatures in the observed data. These spectral signatures are then propagated into the sequence of simulated WRs to the extent justified by the strength of the multinomial logistic regression in equation (3).

3.2. Local Weather Generation Conditioned on WRs

3.2.1. Block Bootstrapping for Multivariate, Multisite Weather Generation

Local weather for the basin of interest is simulated by bootstrapping climate data (e.g., daily precipitation, minimum, and maximum temperature) based on sequences of simulated WRs. Assume that starting on simulation day t , the vector WR contains n days of the i th WR (i.e., WR_t through WR_{t+n-1} equal i). Here, n usually varies from 1 to 14 days, although it can extend longer than 1 month due to the persistence of WRs. To generate weather for those n days, we resample a n^* -day block of historical data that was also classified into the i th WR, where n^* is the longest historical block length available such that $n^* \leq n$. A block is resampled from all M historical blocks of length n^* that also meet two other criteria: (1) the central day of the historical block is within a w -day window of the day of year for simulation day t ($w = \pm 14$ days) and (2) the day prior to the historical block has the same basin-averaged precipitation state as simulation day $t-1$, where basin-averaged precipitation, p_{avg} , is separated into two states: dry ($p_{\text{avg}} = 0$ mm) or wet ($p_{\text{avg}} > 0$ mm). This ensures that the bootstrapped data will preserve the seasonality of local weather and better maintains precipitation persistence across the basin. To resample a block, the M historical blocks are weighted using importance sampling based on a power transformation of the mean basin-averaged precipitation value for the block, so that the mean of the resampled blocks approximates the mean for all blocks associated with state i .

If the length n^* of the resampled block is less than n , then the remaining length $n - n^*$ is used as a basis to resample another block for WR i , and this process is continued until data have been resampled for the entire block of n days. At this point, the WR will change states and the resampling procedure begins again. By using

this block bootstrap procedure, the bootstrapped data are more likely to contain the entire life cycle of a WR, including the birth of an extratropical cyclone over the Pacific and its trajectory over the western United States, preserving the complex space-time structure in resulting weather over the basin of interest.

3.2.2. Copula-Based Jitters

The block bootstrap will preserve many of the properties of the marginal and joint distributions of local weather variables, but at the expense of being able to simulate values outside the range of the instrumental record. We propose a copula-based approach to address this drawback, specifically for precipitation, while maintaining many of the benefits of the block bootstrap. Let $\tilde{\mathbf{p}}_t$ be a vector of simulated precipitation values from the block bootstrap at time t across all sites in the basin. Assume the nonzero precipitation amounts at each site can be modeled by the cdf $F(p|\theta)$. Currently, two forms for $F(p|\theta)$ are permitted in the model: a Gamma distribution or a mixture of exponential distributions. For each simulated day t and site i , let $\tilde{u}_{t,i} = F(\tilde{p}_{t,i}|\theta)$ be the nonexceedance probability associated with $\tilde{p}_{t,i}$. We perturb the values of $\tilde{\mathbf{u}}_t$ to create a new vector of values $\tilde{\mathbf{u}}_t^*$ that are centered around but are not equal to $\tilde{\mathbf{u}}_t$. The perturbations are simulated using a Gaussian copula and are kept small by using a conditional expectation with a conditional correlation matrix that assumes the basin-wide average of precipitation is known. Let Σ be an $(s+1) \times (s+1)$ Spearman (rank) correlation matrix for the vector of daily, observed precipitation $\mathbf{p}_1 : s, \text{avg} = [p_1, \dots, p_s, p_{\text{avg}}]$ that contains all s sites as well as the basin-averaged precipitation. This correlation matrix is estimated based on all precipitation values (including nonzero values) across the entire historical record. Also, let $\tilde{z}_{t,i} = \phi^{-1}(\tilde{u}_{t,i})$ be z-scores (i.e., ϕ is the standard normal cdf) for simulated precipitation at each site and time (but not for the basin-average). A conditional correlation matrix of $\tilde{\mathbf{z}}_t$ assuming the basin-average precipitation is known can then be derived and used to simulate new z-scores $\tilde{\mathbf{z}}_t^*$ from a multivariate normal distribution centered around the original scores:

$$\Sigma_{11|2} = \Sigma_{11} - \Sigma_{12}\Sigma_{22}^{-1}\Sigma_{21} \quad (5)$$

$$\tilde{\mathbf{z}}_t^* \sim \text{MVN}(\tilde{\mathbf{z}}_t, \Sigma_{11|2}) \quad (6)$$

where $\Sigma_{i,j}$ are blocks of the matrix Σ . If the basin-averaged precipitation is highly correlated in rank space with the precipitation at each site, the elements of the conditional matrix $\Sigma_{11|2}$ will be small and $\tilde{\mathbf{z}}_t^*$ will not vary much from $\tilde{\mathbf{z}}_t$. Then, for each site, the perturbed z-score can be back-transformed to a proposed nonexceedance probability, $\tilde{u}_{t,i}^* = \phi(\tilde{z}_{t,i}^*|\theta)$, and an associated proposed precipitation value $\tilde{p}_{t,i}^* = F^{-1}(\tilde{u}_{t,i}^*|\theta)$. The proposed nonexceedance probability will then be selected over the original one based on the following conditional probabilities of observing a different precipitation value given the value that was simulated:

$$\pi = \begin{cases} \Pr(P > \tilde{p}_{t,i}^* | P > \tilde{p}_{t,i}) = \frac{\Pr(P > \tilde{p}_{t,i}^*, P > \tilde{p}_{t,i})}{\Pr(P > \tilde{p}_{t,i})} = \frac{\Pr(P > \tilde{p}_{t,i}^*)}{\Pr(P > \tilde{p}_{t,i})} = \frac{1 - \tilde{u}_{t,i}^*}{1 - \tilde{u}_{t,i}}, \tilde{p}_{t,i}^* > \tilde{p}_{t,i} \\ \Pr(P \leq \tilde{p}_{t,i}^* | P \leq \tilde{p}_{t,i}) = \frac{\Pr(P \leq \tilde{p}_{t,i}^*, P \leq \tilde{p}_{t,i})}{\Pr(P \leq \tilde{p}_{t,i})} = \frac{\Pr(P \leq \tilde{p}_{t,i}^*)}{\Pr(P \leq \tilde{p}_{t,i})} = \frac{\tilde{u}_{t,i}^*}{\tilde{u}_{t,i}}, \tilde{p}_{t,i}^* \leq \tilde{p}_{t,i} \end{cases} \quad (7)$$

$$\tilde{u}_{t,i}^{\text{final}} = \begin{cases} \tilde{u}_{t,i}^* & \pi \leq r_{\text{unif}} \\ \tilde{u}_{t,i} & \pi > r_{\text{unif}} \end{cases} \quad (8)$$

where the random variable P is daily precipitation depth and r_{unif} is a random draw from a uniform distribution between 0 and 1. The final precipitation value is then set equal to $F^{-1}(\tilde{u}_{t,i}^{\text{final}}|\theta)$. If the original block bootstrap precipitation value for a site is zero, it is not adjusted through this procedure. By virtue of the perturbations embedded in $\tilde{\mathbf{z}}_t^*$ and thus $\tilde{\mathbf{u}}_t^*$, the final values of simulated precipitation can extend beyond the range of historical precipitation values, but they preserve the rank correlation structure across sites and the space-time structure captured by the block bootstrap, as long as at-site precipitation is well correlated with basin-average precipitation. In addition, the shape of the underlying distribution of the data is not altered through this procedure (see synthetic experiments in the supporting information).

3.3. Climate Change Perturbations for Vulnerability Assessments

We adopt an approach where climate perturbations are imposed separately for thermodynamic and dynamical processes, enabling a clearer link between local climate changes and their associated causal pathways. We argue that this strategy is well suited to facilitate the use of climate science to constrain and inform the likelihood of future climate changes tested in the vulnerability assessment.

3.3.1. Thermodynamic Perturbations

3.3.1.1. Temperature Trends

Temperature change is treated simply by adding trends to simulated temperature data for each location across the spatial domain. Currently, only step changes are permitted, but linear or quadratic trends are also possible. An option for elevation dependent warming is also available. Elevation-dependent warming is not clearly observable in ground-based observations below 2,000 m asl (Pepin & Lundquist, 2008; Rangwala & Miller, 2012). However, surveys of both GCM output (Rangwala et al., 2016) and ground-based observations (Pepin et al., 2015) show that above 2,000 m, each additional kilometer of elevation increases the rate of warming between 5% and 50%. Accordingly, temperature perturbations in this weather generator allow elevation-dependent warming up to 50% per kilometer of elevation over a baseline level of warming for elevations below 2,000 m asl.

3.3.1.2. Daily Precipitation Scaling

We use quantile mapping to scale the distribution of precipitation in a way that replicates the effects of warming temperatures on precipitation through increases in the moisture holding capacity of the atmosphere, that is, CC scaling. Similar to other studies (Pendergrass & Hartmann, 2014b), we quantify CC scaling as a percent change in the moments and quantiles of the precipitation distribution per degree warming. Separate scaling rates are selected for the mean and the 99.9th percentile of non-zero precipitation. New parameters $\{\theta_{CC}\}$ of $F(p|\theta)$ are determined by optimizing a vector of multiplicative perturbations δ to the parameters (i.e., the Hadamard [element-wise] product $\theta_{CC} = \delta * \theta$) to impose the selected scaling rates. Once the new parameters are determined for each site and month, daily simulated precipitation $\widetilde{p}_{t,i}$ is adjusted by first determining the nonexceedance probability $\widetilde{u}_{t,i} = F(\widetilde{p}_{t,i}|\theta)$, then perturbing the nonexceedance probability into $\widetilde{u}_{t,i}^{\text{final}}$ using the copula-based model above, and finally determining a new precipitation value based on the CC-scaled distribution: $\widetilde{p}_{t,i}^{\text{final}} = F^{-1}(\widetilde{u}_{t,i}^{\text{final}}|\theta_{CC})$. This procedure is repeated for each nonzero precipitation amount for each site synthesized by the weather generator.

Importantly, the degree to which precipitation is scaled is directly tied to the temperature trends imposed, thus respecting the underlying thermodynamic mechanism that drives CC scaling. That is, precipitation scaling in the model is entirely determined after specifying a temperature trend and a scenario of CC scaling per degree warming. In this way, emerging hypotheses related to regional warming and CC-scaling relationships, which are arguably less uncertain than precipitation changes linked to dynamical processes (Pfahl et al., 2017), can be directly tested with respect to their impact on water systems. For the 99.9th percentile, we recommend a range of possible CC-scaling rates from 1-3×CC-scaling (i.e., 7-21% C⁻¹) based on a survey of the literature (Bao et al., 2017; Fischer & Knutti, 2016; Guerreiro et al., 2018; Lenderink et al., 2017; Trenberth, 2011; Westra et al., 2014). For mean precipitation, a range from -1 to +1×CC-scaling (-7% to +7% C⁻¹) is recommended over land in the midlatitudes based on empirical evidence from multimodel ensembles (Emori & Brown, 2005; Hawcroft et al., 2018; Li et al., 2013) and recent advances in theoretical scaling laws for surface water availability (mean precipitation less evaporation, P-E; Held & Soden, 2006; Seager & Vecchi, 2010; Seager et al., 2010; Boos, 2012; Byrne & O’Gorman, 2015; Ting et al., 2018). These studies highlight constraints on mean precipitation thermodynamic scaling due to limiting rates of atmospheric cooling (Allen & Ingram, 2002; Muller & O’Gorman, 2011; Pendergrass & Hartmann, 2014a). In addition, they suggest that declines in P-E (and P only) are possible over land due to changes in atmospheric water vapor gradients that could reduce moisture convergence, particularly near land-ocean boundaries like the western United States.

3.3.2. Dynamical Perturbations

To impose dynamical climate change, we change the frequency of different WRs through perturbations to the transition probabilities that control the evolution of the Markov chain. These parameters could be perturbed directly to make different WRs more or less likely compared to their historical frequency. An alternative strategy, and the one taken in this study, is to change the behavior of quasi-oscillatory climate

patterns like ENSO that influence WR frequency. We specifically test an emerging hypothesis that the frequency of extreme El Niño and La Niña events is going to increase under climate change (Cai et al., 2014, 2015). This change is simulated by increasing the variance of the low-frequency component of the Niño 3.4 index in the WARM model.

4. Model Evaluation

To evaluate the model, we first examine the identified WRs, including their transition properties, seasonality, and relationship to ENSO. Then we examine how well simulations reproduce characteristics of the weather over the Tuolumne River Basin. This latter analysis is repeated twice, once using the full model (i.e., multinomial logistic regression and WARM model of Niño 3.4) and once conditioned on the historical WR sequence, in order to better isolate the strengths and limitations of the bootstrap and the model of WRs. All results are based on a 200-member ensemble of 38-year simulations to match the length of the historical record. After an initial assessment we choose to model the distribution of daily nonzero precipitation ($F(p|\theta)$) using a Gamma distribution, although results vary only slightly if a mixed exponential distribution is used instead.

4.1. Weather Regimes

Based on scree tests, we select the first nine EOFs of standardized 500-hPa height anomalies over the Pacific/North American sector, which explain over 90% of the data variance, and cluster the associated PCs into eight different WRs (see Figures S1 and S2 in the supporting information). Figure 3 shows composites of 500-hPa height and IVT anomalies for all days classified into each WR. The eight different WRs show substantial differences in large-scale atmospheric flow across the Pacific Ocean, North American coastline, and continental interior, which will have important implications for weather variability experienced locally in the western United States. For instance, WR 7 exhibits a strong anomalous trough south of Alaska and significant moisture flow toward the Sierra Nevada in California, suggesting that this WR is associated with landfalling ARs and heavy precipitation along the California coastline. Indeed, based on the AR database of Brands et al. (2017), the most landfalling ARs along the western U.S. coastline occur during days classified as WR 7 (see Figure S3). WR 6 shows a cutoff low over the southwest United States and strong, meridional moisture transport from the eastern subtropical Pacific. The pattern has been associated with ARs that impact key river basins in the Southwest, such as the Salt and Verde Basins (Rivera et al., 2014; Steinschneider et al., 2018), and so likely impacts surface weather in that location. In contrast to WRs 6 and 7, WRs 1 and 5 exhibit a ridge over most of the western United States that diverts moisture flow further to the north toward the Pacific Northwest and Canada. This pattern resembles the “Ridiculously Resilient Ridge” that caused the 2011–2016 California drought (Seager et al., 2015) and therefore is likely associated with dry, warm conditions in many parts of California.

To determine the homogeneity of atmospheric flow within each WR, Figure 4 shows a reclustering of the nine PCs for all days that were classified as WR 7. Similar results are presented for other WRs in Figures S4–S10. For WR 7, all subclusters exhibit the same trough south of Alaska, but the precise position and orientation of the trough shift between subclusters. Accordingly, the direction and strength of IVT also change across subclusters, which will cause shifts in precipitation for different locations along the western U.S. coastline. Therefore, even within a particular WR, surface climate for a particular river basin will still likely exhibit significant variability. The effect of the WR is rather to enforce a shift in the odds of particular types of events (heavy rains, dry conditions), rather than to completely predict their occurrence.

This effect is clearly seen when examining the distribution of daily precipitation averaged across the Tuolumne River Basin, conditional on each of the 8 WRs (Figure 5). The distributions of precipitation by WR show clear shifts that align with expectations based on shifts in atmospheric flow (see Figure 3). For example, daily precipitation is much more likely to be heavy or extreme during WR 7, when ARs often make landfall along the California coastline, but it is highly likely to see little or no precipitation under WR 1, when a ridge is situated over the western U.S. However, Tuolumne precipitation can still vary substantially within a particular WR. This is in part due to differences in atmospheric flow within a particular WR (see Figure 3 and S4–S10), but it is also caused by the fact the full life cycle of an extratropical cyclone, including its formation over the ocean and trajectory

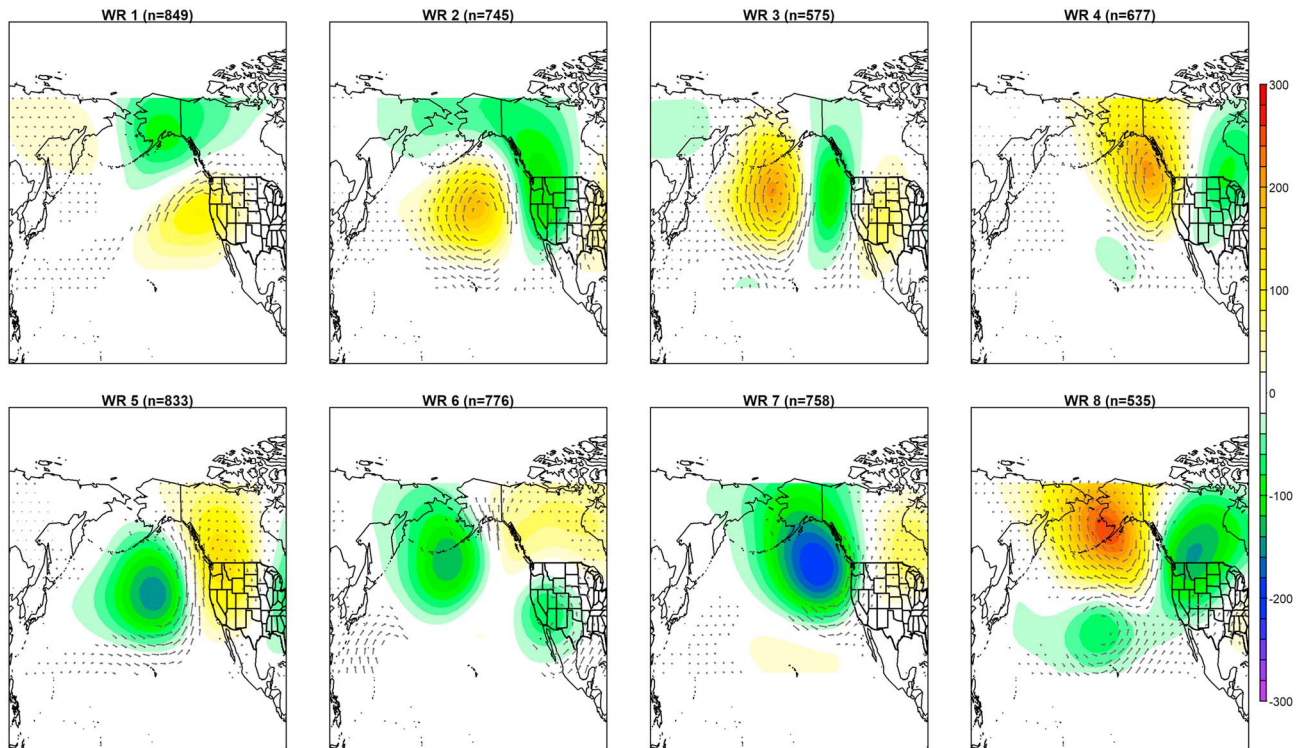


Figure 3. Atmospheric flow composited over days classified under each weather regime, including anomalies of 500-hPa geopotential height (shaded) and integrated water vapor transport (arrows). Integrated water vapor transport is only shown when it exceeds its mean seasonal value. The number of days (n) in each weather regime (WR) is also provided.

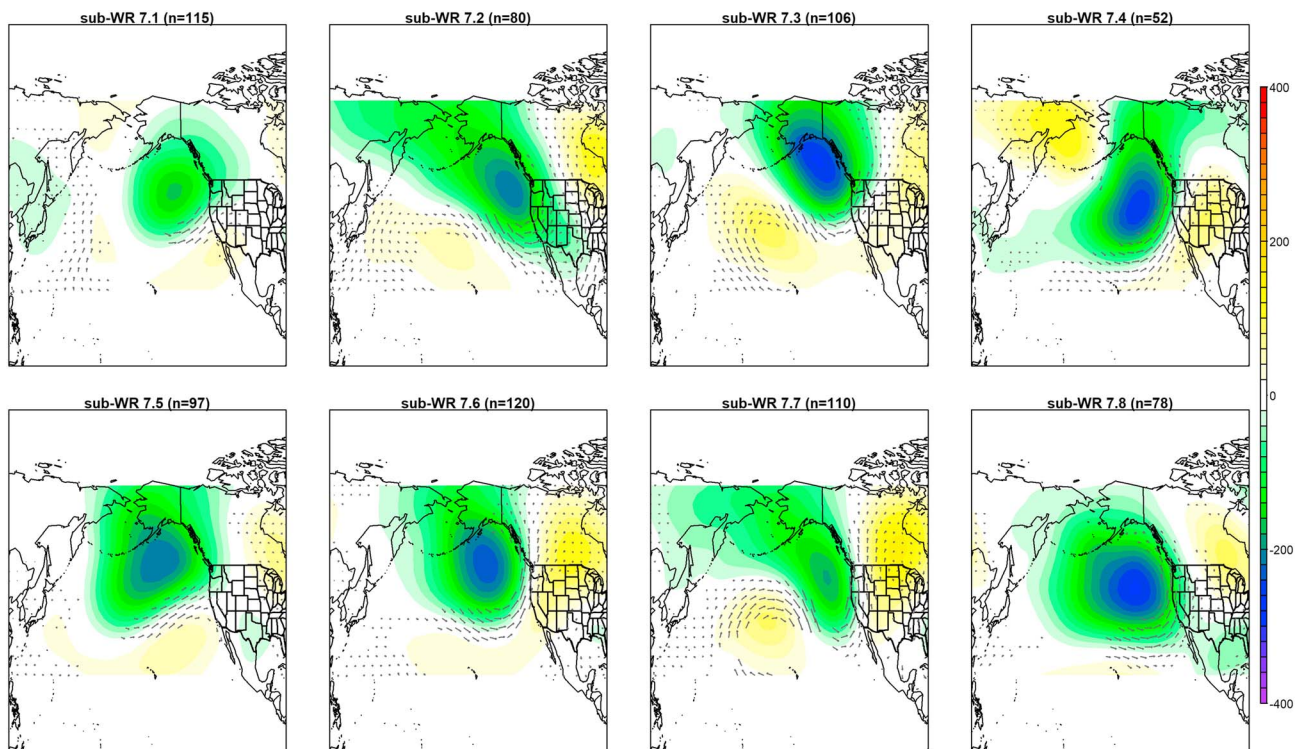


Figure 4. Atmospheric flow composited over days classified under each sub-cluster for weather regime (WR) 7, including anomalies of 500-hPa geopotential height (shaded) and integrated water vapor transport (arrows). Integrated water vapor transport is only shown when it exceeds its mean seasonal value. The number of days (n) in each subcluster is also provided.

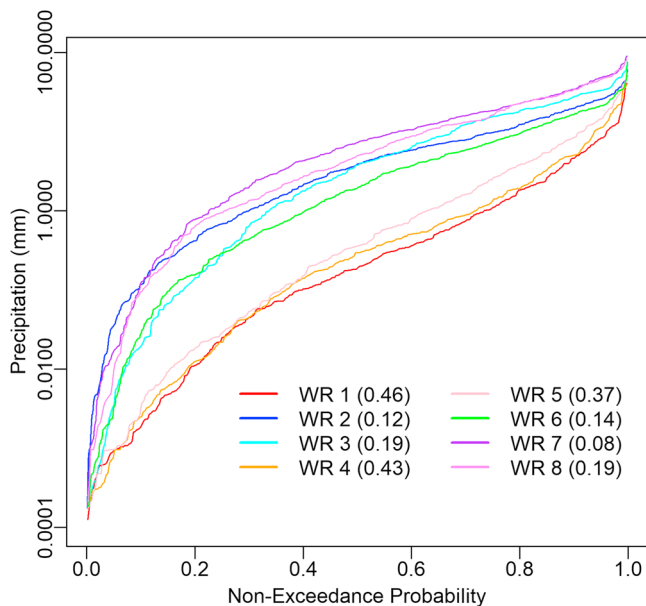


Figure 5. The distribution of non-zero basin-average precipitation across the Tuolumne River Basin under each weather regime. The probability of a dry day under each weather regime (WR) is also provided.

over land, can elapse during a single WR. This motivates the use of block bootstrapping in daily weather generation, to capture the evolution of storms within a particular WR and their impact on specific regions of the western U.S.

The dynamics of WR transitions span multiple time scales. Tables S1 and S2 in the supporting information show the steady state probabilities and homogeneous transition probability matrix across WRs. At daily to weekly scales, the WRs exhibit significant persistence (self-transition probabilities between 63 and 75%) and have similar steady state probabilities (between 9 and 15%), with WRs 1 and 8 occurring most and least frequently, respectively. At seasonal time scales, the frequency of most WRs remains relatively constant, although WR 3 tends to become less frequent in the middle of the cold season, while WR 4 becomes more frequent during that time (Figure 6). At interannual timescales, ENSO significantly modulates the likelihood of certain WRs, although some others are less affected. For instance, WRs 5, 6, and 7 are more likely to occur during El Niño events, while WRs 1, 2, and 3 are more prevalent during La Niña (Figure S11). The significance of these effects for the Markov chain simulation is more clearly seen in Figure 7, which shows results from the multinomial logistic regression for transition probabilities conditioned on the Niño 3.4 index, given that the previous day was WR 1 (chosen for illustration). Consistent with the negative correlation between the Niño 3.4 index and WR 1 occurrences (see Figure S11), these

results show a significant decline in the persistence of WR 1 under strong El Niño conditions, and a decrease in the transitions from other WRs into WR 1. This will result in fewer (more) simulated WR 1 occurrences in a year in which El Niño (La Niña) conditions are simulated to occur.

Simulations of the Niño 3.4 index are based on the WARM model. Figure 8 shows the time series of historical Niño 3.4 values, the associated power spectrum, and the global power spectrum. The historical time series exhibits a significant signal in the 4- to 6-year band, which is well simulated by the WARM model, as shown by the mean global power spectrum of 200 simulations. The ensemble of WARM simulations also captures the variance of the historical process well.

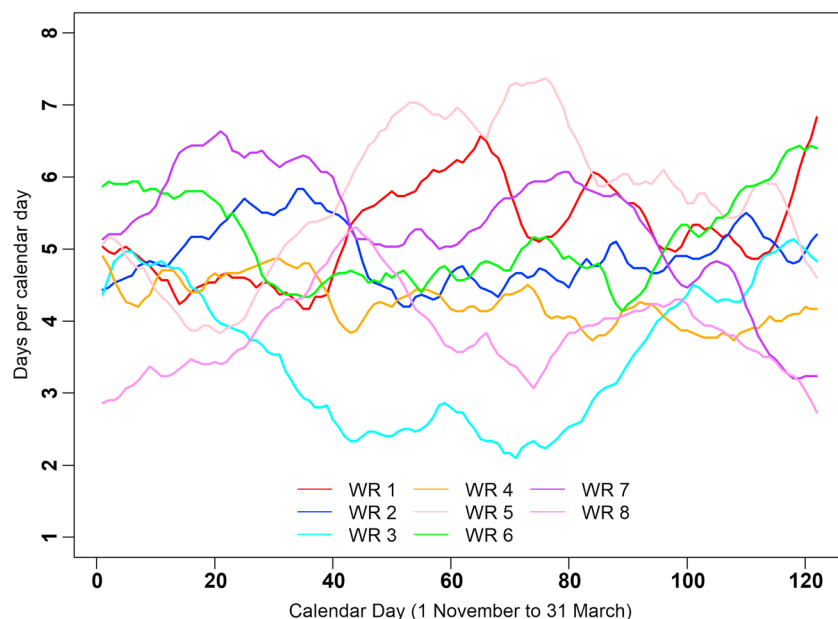


Figure 6. The frequency of each weather regime (WR) through the cold season, shown as a 30-day moving average of the number of WR occurrences for each calendar day between water years 1980 and 2017.

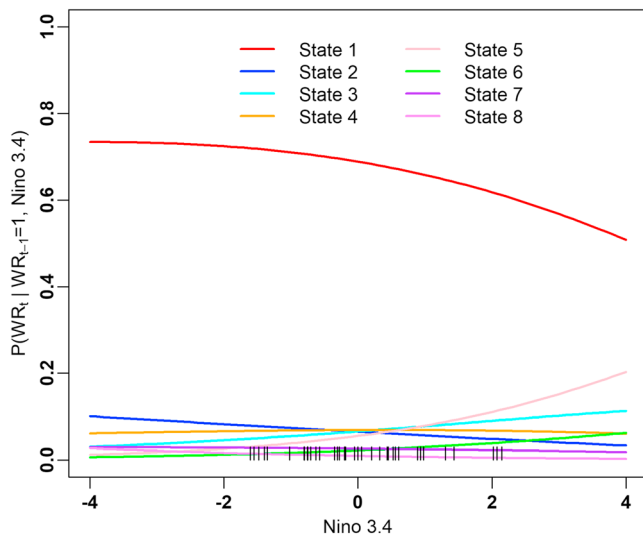


Figure 7. Transition probabilities from weather regime (WR) 1 to the other WRs, conditioned on the Niño 3.4 index through a multinomial logistic regression. Historical values of December–February Niño 3.4 used in model fitting are also shown.

4.2. Tuolumne Weather

Figure 9 shows observed versus simulated precipitation statistics in the Tuolumne Basin based on the full model, along with the simulated ensemble spread. Results are shown for each of the grid cells (i.e., at-site statistics), as well as for basin-average statistics. Similar results for simulations based on historical WRs are presented in Figure S12. Overall, many of the historical statistics are well preserved in the simulations, including the at-site mean, variance, and skew. The maximum precipitation value at each site is also well preserved, and the spread in the simulations extends well beyond the historical maxima due to the use of copula-based jitters. The simulated probabilities of wet (dry) days are slightly overestimated (underestimated), and the average wet and dry spell lengths tend to be negatively biased by between 1 and 2 days. Maximum wet and dry spells are also underestimated, although variability in the model can create maximum wet spell lengths that exceed the historical maximum for many sites. This is also the case for some sites and maximum dry spell lengths, although maximum dry spells are significantly underestimated at other sites.

A comparison between simulations using historical (Figure S12) and modeled (Figure 9) WRs suggests that the formulation of the block bootstrap and not the ENSO-informed model of WRs is the source of error in spell

statistics. This limitation, discussed further in section 6, is also likely the cause of the negative bias in the variance of cold season precipitation totals across sites and in the basin average. Despite this limitation, the at-site and basin skew in cold season precipitation is relatively well simulated, as is the seasonal cycle. The rank correlation of precipitation across sites (including nonzero values) is well simulated, although slightly underestimated for the pairs of sites with lowest correlation. Some but not all of this underestimation is removed if copula-based jitters are not used, but at the expense of maximum simulated precipitation that is limited to the historical maximum (see Figure S13).

A similar comparison for daily maximum temperature is presented in Figure 10 (Figure S14 for historical WRs). Results for daily minimum temperature are very similar and thus omitted. Similar to precipitation, the moments and extremes of daily maximum temperature are well simulated. Also, similar to precipitation, simulated lag 1 autocorrelation and the variance of cold season maximum temperature are negatively biased as a result of the block bootstrap as opposed to the ENSO-based model of WRs. Cold season skew, cross-correlations across sites, and the basin-averaged seasonal cycle are all well preserved.

Finally, Figure 11 shows the observed and simulated rank-based cross correlations between daily precipitation (zero and nonzero values) and maximum temperature by site and across months. Overall, these cross correlations are well preserved in the simulations, particularly for the primary winter months, although the simulations have a tendency to slightly underestimate the strength of the correlation. Deviations between the observed and simulated values are primarily driven by small biases in the number of wet and dry days (see Figure 9) as well as perturbations to precipitation that were imposed through the copula-based jitters.

5. Demonstration of Scenario Development for Vulnerability Assessments

The weather generator is designed to support a thorough exploration of water system sensitivities to perturbations in the underlying climate system directly linked to thermodynamic and dynamical forms of climate change. We demonstrate three different perturbations over the Tuolumne basin: (1) a thermodynamic CC-scaling of daily precipitation, (2) the spatial distribution of elevation dependent warming, and (3) a dynamical change to the frequency of extreme ENSO events.

Figure 12 shows the changes to the distribution of nonzero daily precipitation at one grid cell in January associated with four different scenarios of change: 1°C warming and 1 × CC scaling in the upper quantiles of daily nonzero precipitation with mean scaling of 0% and 3% per °C, 1°C warming and 2 × CC-scaling with

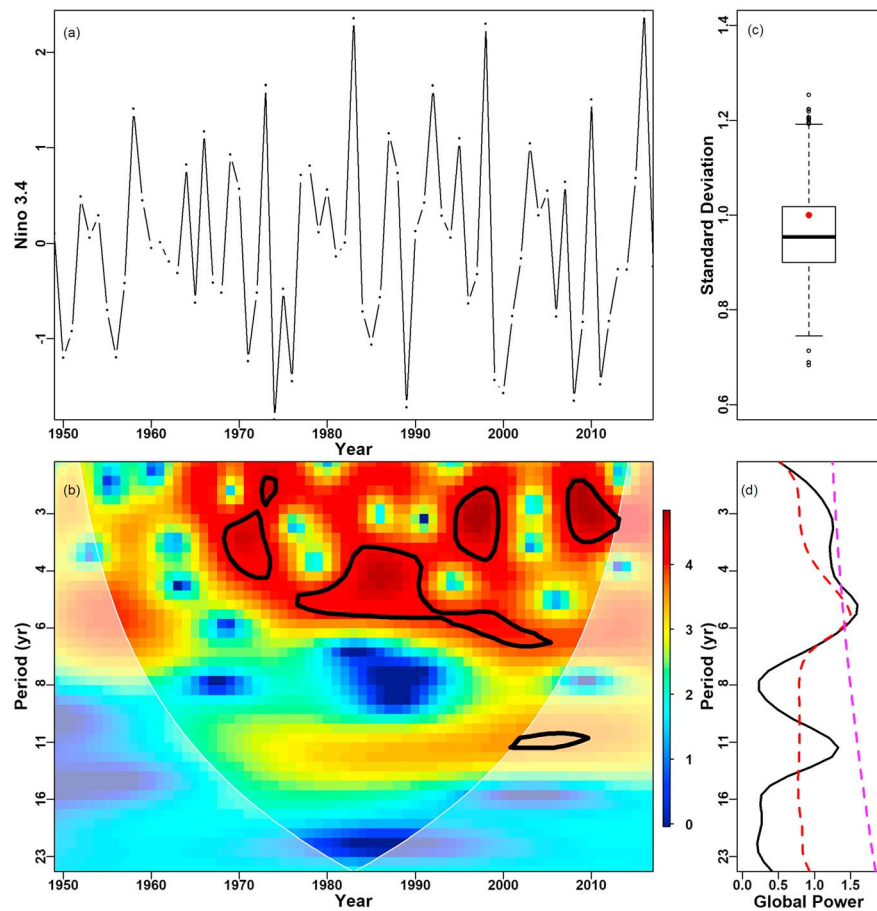


Figure 8. Wavelet autoregressive model (WARM) results for the December-February Niño 3.4 index. (a) Time series and (b) power spectrum of the historical Niño 3.4 index. In (b), statistical significance at the 90% level is shown as bolded contours for a red-noise background process. (c) The standard deviation of the 200 WARM-simulated Niño 3.4 time series, along with the observed standard deviation. (d) The global power spectrum of the observed Niño 3.4 index (black) and the mean global power spectrum of 200 WARM-simulated time series (red), along with a 90% significance level based on a red-noise background process (pink).

no mean change, and 2°C warming and 2 × CC-scaling with no mean change. These scenarios are compared against a baseline model run with no changes imposed, with differences to baseline expressed as a percent change in the empirical quantiles of the data from both scenarios.

When the mean value is left unchanged, a 1°C warming and 1 × CC-scaling in the upper quantiles causes the distribution to stretch, such that the highest events (>0.80 nonexceedance level) are increased and the remaining, smaller precipitation values are decreased in order to maintain the same mean value (Figure 12a). These changes are consistent with past work describing how the full distribution of precipitation will likely change in a warming world (Fischer & Knutti, 2016; Pendergrass & Hartmann, 2014b). The degree of stretching follows the amount of CC-scaling and the temperature increase, with 2 × CC-scaling under 1°C and 2°C warming producing extreme precipitation events that are 14% and 28% higher than similar events under the baseline distribution, respectively (Figures 12b and 12c). If the mean of daily precipitation is also permitted to scale with temperature (e.g., 3% per °C), more of the precipitation distribution (>0.30 nonexceedance level) is elevated above baseline values to accommodate the mean increase, although tail events still only increase by 7% under 1°C warming and 1 × CC scaling (Figure 12d).

It is worthwhile to note that the change in the mean in some scenarios is biased approximately 1% below the change that is expected. This small bias is also seen in synthetic experiments based on random sampling from a gamma distribution that was used to test the copula-based jitters and arises only with large

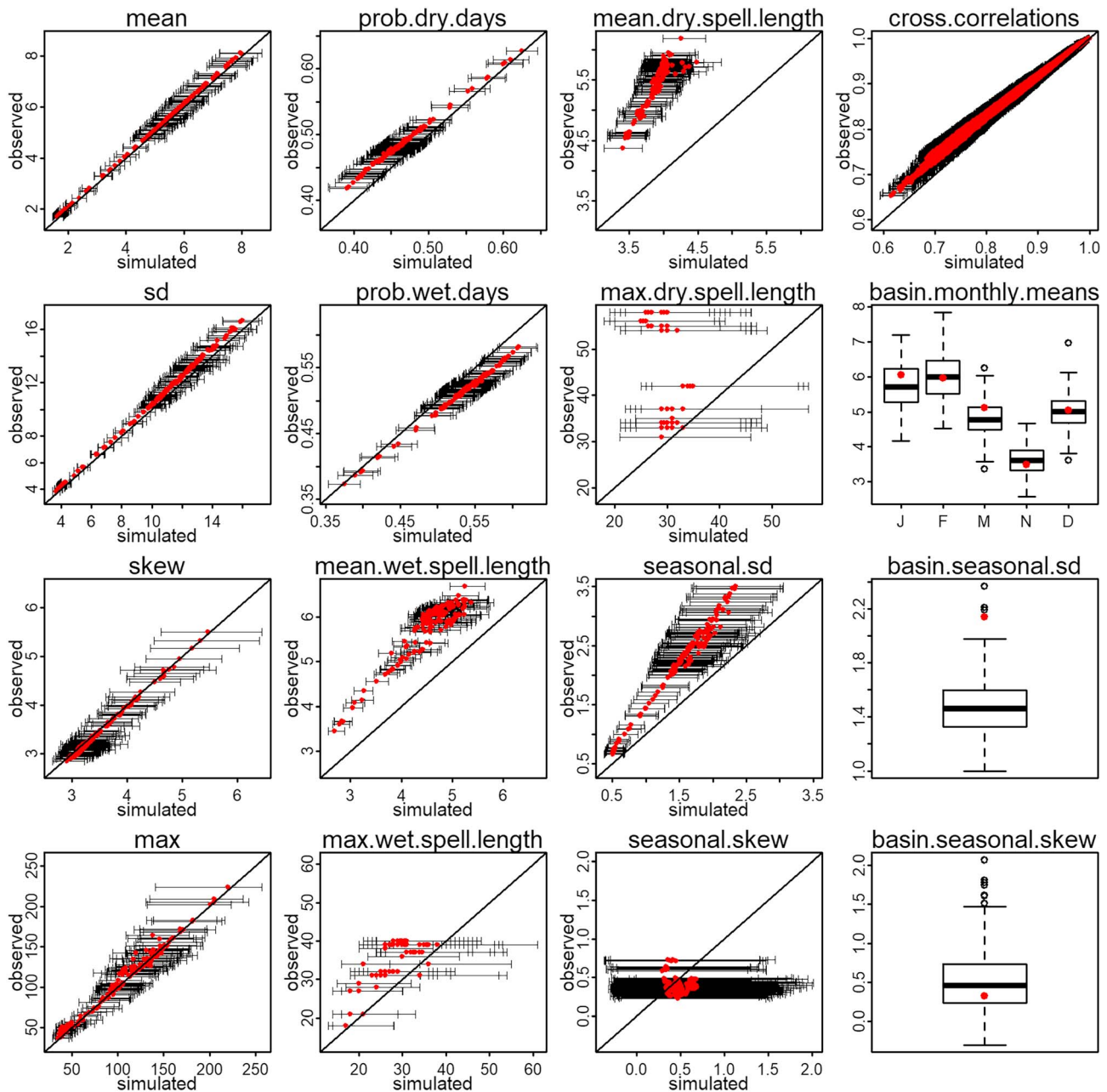


Figure 9. Observed vs. simulated characteristics of daily precipitation in the Tuolumne Basin, where daily simulations are based on weather regimes conditioned on wavelet autoregressive model-simulated time series of Niño 3.4. For at-site characteristics (160 grid cells), the 95% range for simulated statistics across the 200 ensemble members is shown with whiskers. For basin-averaged statistics, the distribution of simulated statistics is shown as a boxplot along with the observed value.

conditional variances in equations (5) and (6) (Figure S15). This bias is constant regardless of the change in the mean or upper quantile that is imposed (Figures S16 and S17) and does not extend to any of the quantiles of the distribution.

Figure 13 illustrates the impact of three levels of elevation-dependent warming on a scenario of +1 °C temperature increase in the Tuolumne basin. Elevations in the Tuolumne basin range from approximately 30 to 4,000 m asl. If, for example, a temperature perturbation of +1 °C is applied to all parts of the watershed below 2,000 m asl, and 50% additional warming is applied for each km above 2,000 m asl, then elevations near 3,000 m asl will receive 1.5 °C warming and elevations near 4,000 m will receive 2 °C warming.

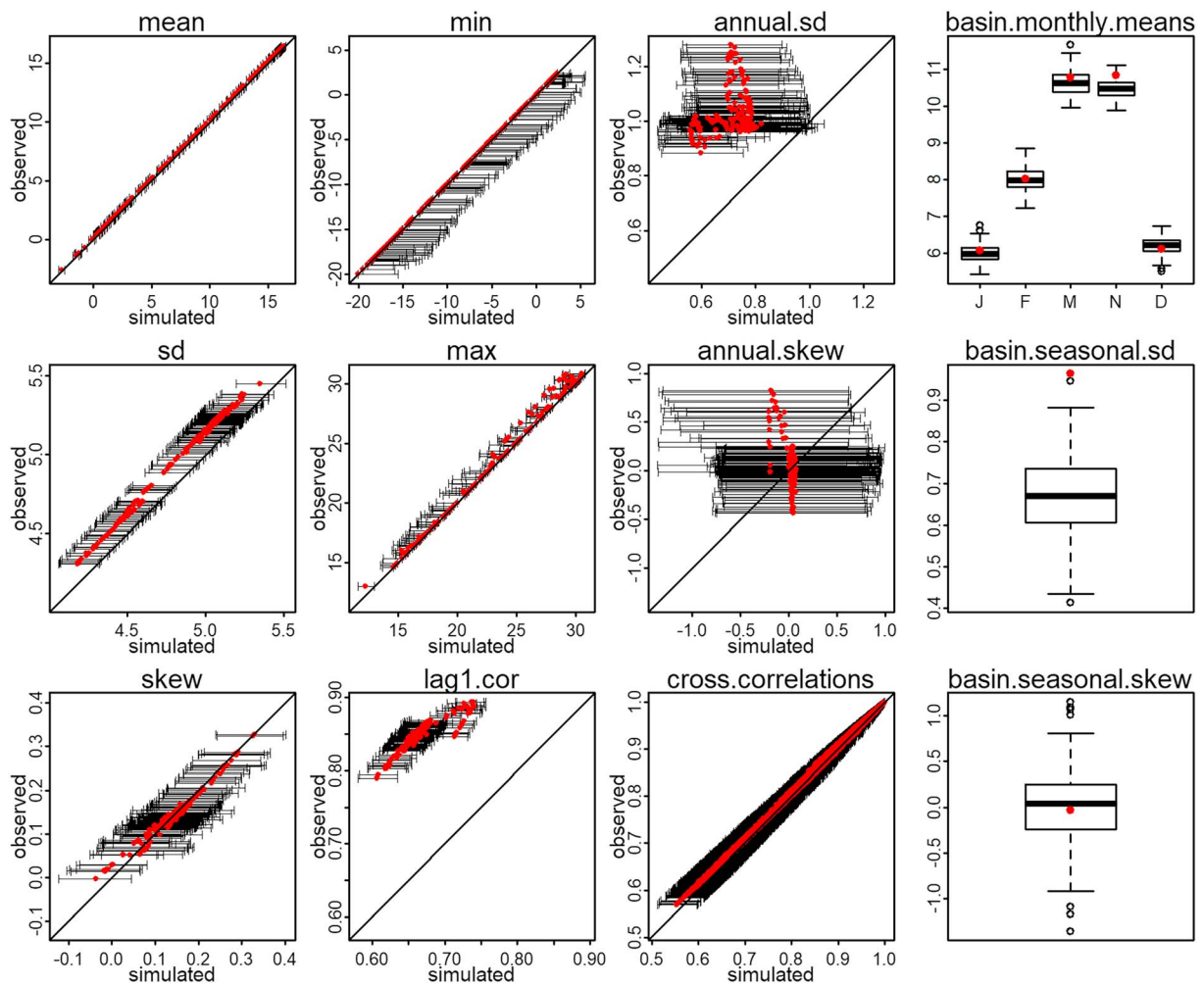


Figure 10. Observed vs. simulated characteristics of daily maximum temperature in the Tuolumne Basin, where daily simulations are based on weather regimes conditioned on wavelet autoregressive model-simulated time series of Niño 3.4. For at-site characteristics (160 grid cells), the 95% range for simulated statistics across the 200 ensemble members is shown with whiskers. For basin-averaged statistics, the distribution of simulated statistics is shown as a boxplot along with the observed value.

Lower rates of elevation-dependent warming are possible on a continuous scale from +0 to +50%/km (e.g., +5 or +25%/km as shown in Figure 13). We note that existing temperature trends in the Tuolumne do exhibit elevation-dependent warming, particularly for minimum temperatures in the cold season (Figure S18), consistent with previous work (Pepin et al., 2015; Rangwala et al., 2016).

A complete picture of local climate change depends not only on thermodynamic change but also on dynamical changes that manifest as shifts in WR frequencies and the associated characteristics of local weather (e.g., frequency of wet days). This is explored in Figure 14, which shows how changes in the variance of the Niño 3.4 index impact the mean and variance of basin-averaged seasonal precipitation. Although we alter the variance of the low-frequency component of the WARM model for the Niño 3.4 index, we report the change in variability for the final simulated Niño 3.4 index for clarity. For this demonstration, we create a scenario in which the standard deviation of the Niño 3.4 index is doubled, which likely serves as a limiting scenario for potential changes to ENSO variability under climate change (Cai et al., 2015).

Figure 14 shows that the mean of seasonal precipitation increases modestly with additional ENSO variability, with an average increase of 5% over the ensemble. This suggests a slight asymmetric response in regional precipitation to strong El Niño and La Niña events, consistent with past work (Hoerling et al., 2001). The standard deviation in basin-averaged precipitation increases more than the mean as the ENSO process

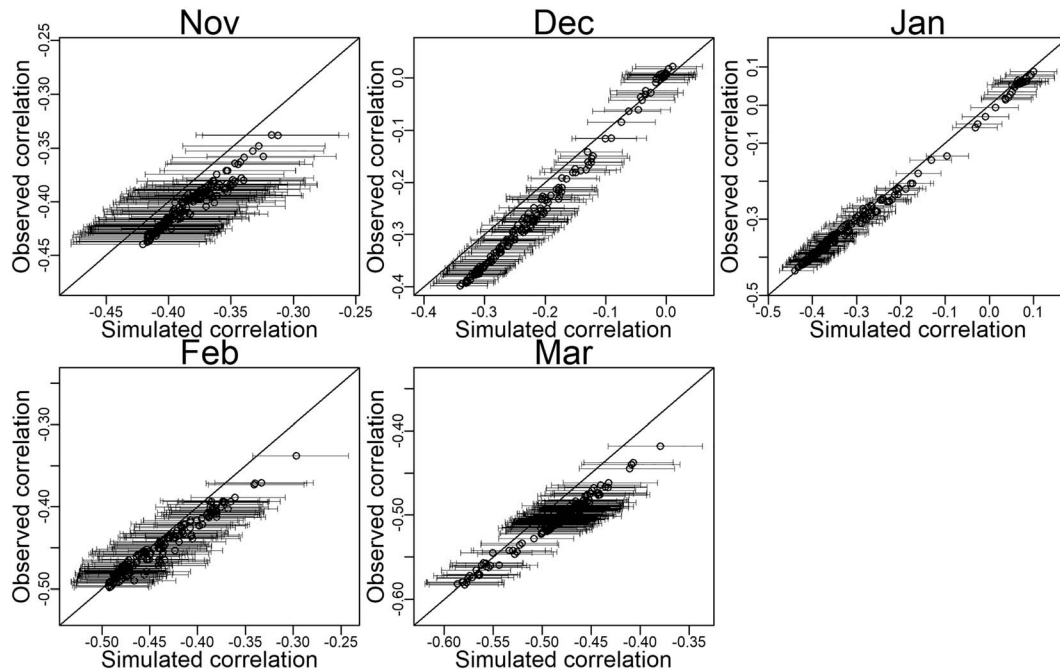


Figure 11. Observed vs. median simulated Spearman cross correlations between daily precipitation and maximum temperature at each site by month. The 95% range for simulated cross correlations across the 200 ensemble members is shown with whiskers.

becomes more variable, but still at a limited rate. Even if the standard deviation of the Niño 3.4 index is doubled, the average increase in the standard deviation of seasonal precipitation is only 11%. This is likely because the Tuolumne Basin is located in central California, rather than in southern California where the primary impacts of the ENSO teleconnection are experienced (Hoell et al., 2016). The range of change in standard deviation across the 200-member ensemble is large (−40 to 100%), suggesting that natural variability in basin-wide precipitation, likely linked to mid-latitude dynamics (i.e., WR transitions) unrelated to ENSO, dominates the variability of local precipitation. Hence, the weather generator is able to show how changes in the ENSO process have a significant but relatively small effect on the climate in the Tuolumne Basin, at least based on historical teleconnections. This insight would then help alleviate concerns regarding ENSO in a broader climate vulnerability assessment, motivating a shift in focus to other aspects of climate change to which the system is more sensitive.

6. Discussion

The WR-based stochastic weather generator proposed in this study is designed to be a flexible tool that can facilitate computationally fast, internally consistent scenario generation to support climate vulnerability assessments of water systems in a way that is more easily connected to advances in climate science. The tool is also well suited for risk-based simulation studies of system-of-systems that span large regions and multiple sectors (e.g., food, energy, and water). For instance, the California water and energy sectors are influenced by renewable energy and water resources produced throughout the state and imported from other regions like the Colorado River Basin (water) and Pacific Northwest (hydropower energy). The WR-based model presented here would be capable of generating internally consistent climate scenarios across large regions and multiple variables needed for such analyses, using the WRs as an organizing principle to maintain relevant spatial and temporal structure in the data.

Furthermore, the WR-based stochastic weather generator may prove useful in expediting the adoption of bottom-up vulnerability assessments across water, food, and energy sectors, by providing a regional set of scenarios that can be tailored for individual locations and analyses. Such an approach has proven successful in the past. In 1982, the Hydrology Subcommittee of the Interagency Advisory Committee on Water Data published Bulletin 17B, in which they described an approach to flood frequency analysis where regional

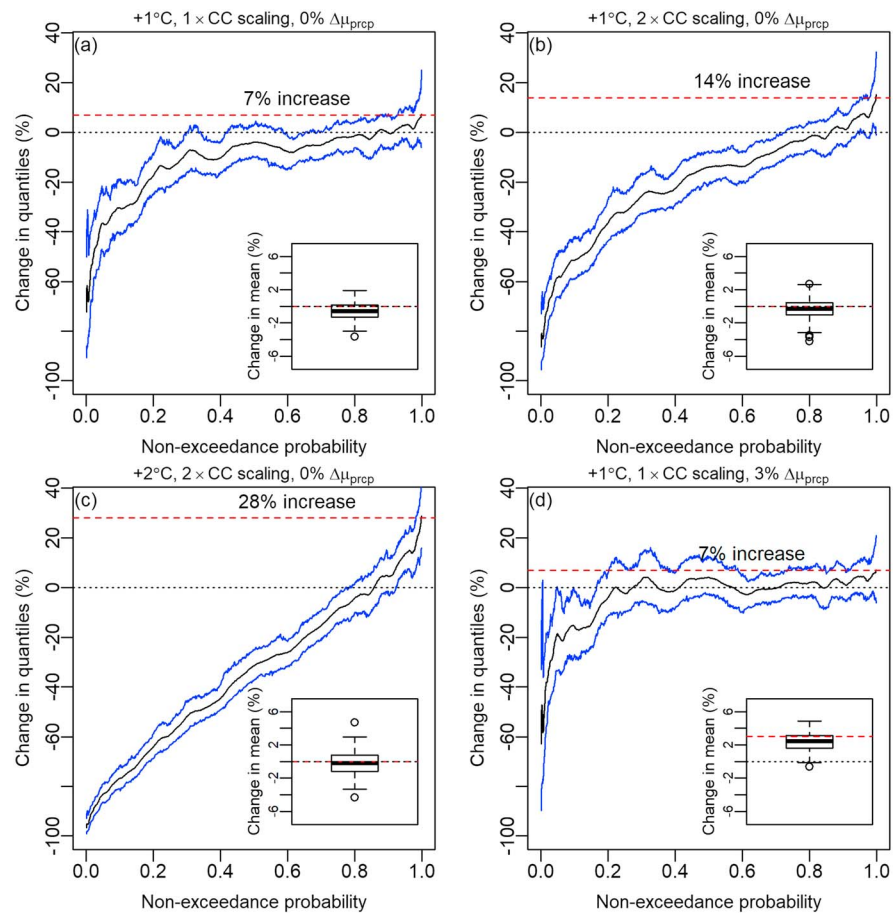


Figure 12. The change in daily nonzero January precipitation distributions between scenarios of thermodynamic change and a baseline, expressed as a percent difference from baseline for quantiles of the distribution. Four scenarios are shown: (a) 1°C warming, 1 × CC-scaling, 0% per °C mean scaling; (b) 1°C warming, 2 × CC-scaling, 0% per °C mean scaling; (c) 2°C warming, 2 × CC-scaling, 0% per °C mean scaling; and (d) 1°C warming, 1 × CC-scaling, 3% per °C mean scaling. The median change (black) is shown along with 95% confidence bounds (blue) across the 200-member synthetic ensemble. The expected change in the 99.9th percentile is shown in red. (inset) The distribution across the ensemble of percent changes in mean nonzero precipitation between the two scenarios. Again, the expected change is shown in red.

skew information could be combined with an at-site analysis to develop more precise estimates of key design events. In this way, the analysis of flood risk was effectively divided between a dedicated team of experts that examined regional-scale flooding patterns and individual analysts that used that regional information to inform site-specific studies. We argue that the proposed WR-based stochastic weather generator can serve a similar purpose. Scenarios of dynamical climate change can be advanced through a focused investigation of WR dynamics and their response to large-scale changes in the climate system. These scenarios, developed by a dedicated team of regional climate experts, can be made publicly available and coupled with open source software to generate synthetic weather data that are tailored for any location across the western United States and the needs of individual water management agencies. This would establish a hierarchical strategy to scenario development that could help expedite and unify climate vulnerability analyses for water systems across the West and help advance the approach as a standard of practice in the field.

While the hierarchical structure of the proposed weather generator has many potential benefits, the model does have several drawbacks that require discussion. First, embedded in the underlying model structure is an assumption that WRs are fixed in space and their underlying canonical structure and influence on local weather will remain unchanged. Rather, climate change will only impact the frequency of these atmospheric flow patterns. However, there is evidence that storm tracks will shift poleward with climate change

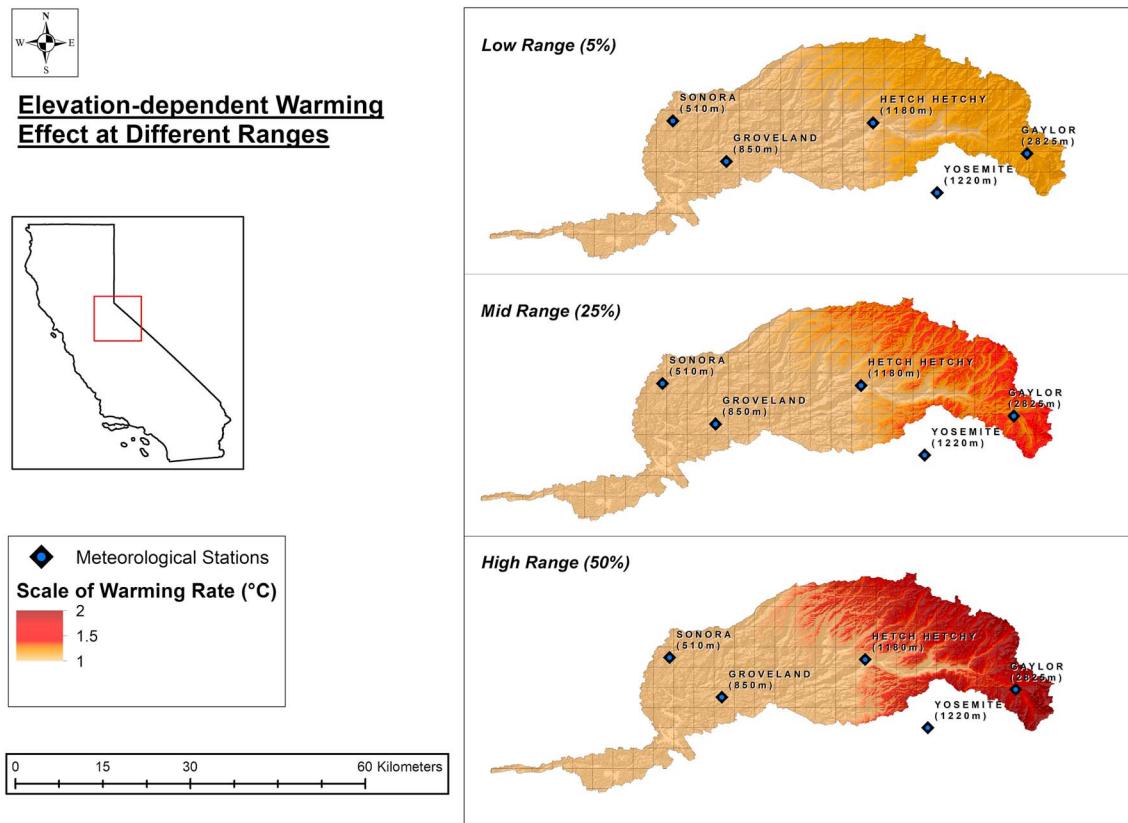


Figure 13. Effect of elevation-dependent warming (+5, +25, and +50%/km) on +1 C temperature perturbation.

(Seager et al., 2014) and that the link between WRs and certain types of storms could change under warming (Mallet et al., 2017). Additional work is required to determine whether this type of change can be modeled effectively as a change in the frequency of previously observed WRs, or if entirely new WRs are needed to capture such a climate shift. If the latter proves true, then the proposed approach to WR simulation would need to be adapted to capture the plausible range of dynamical climate change. Additional analysis following the work of Muñoz et al. (2017) would help to better understand how GCM simulations reproduce and then project changes in WRs across the Pacific North American sector.

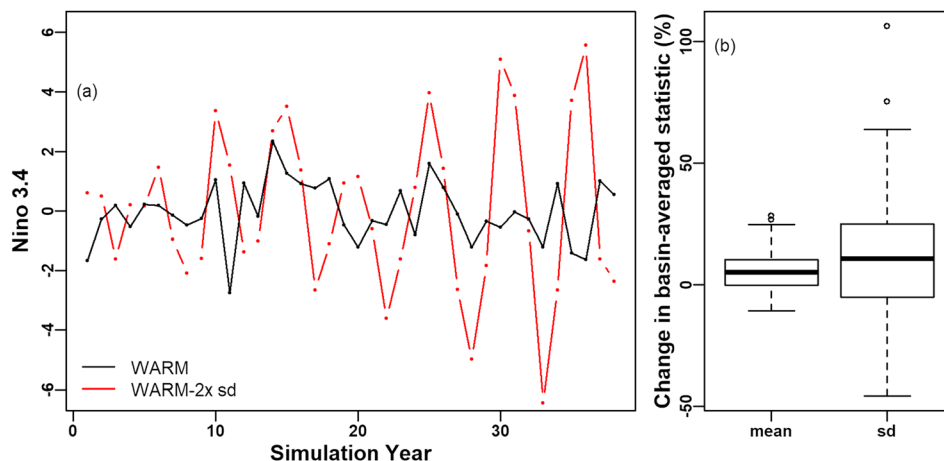


Figure 14. (a) One simulation of the Niño 3.4 index using the original wavelet autoregressive model and the model with a variance inflation factor for the low-frequency component that effectively doubles the standard deviation of the index. (b) The 200-member ensemble distribution of change in the mean and standard deviation of cold season precipitation averaged across the Tuolumne Basin between the original and variance inflated wavelet autoregressive model runs.

In addition, although most statistics of local weather in the Tuolumne River case study were well simulated by the model, others (e.g., spell statistics) could be improved through modifications to the bootstrapping algorithm or the use of different algorithms altogether for the simulation of local weather. One option would be to use a parametric approach, such as transformed, censored latent Gaussian fields with an autoregressive component (Sparks et al., 2018). Such approaches have also shown promise for hourly simulation (Allard & Bourotte, 2015) and therefore could be used to extend the use of the weather generator for detailed vulnerability assessments of flood risk. Furthermore, the current formulation of copula-based jitters may reduce or eliminate tail dependencies between simulated precipitation extremes due to its use of a Gaussian copula. However, the jitters could be produced using a Student-t copula with scale matrix conditioned on the basin average (see Käärik et al., 2011), which would better preserve tail dependencies. Similarly, different distributions for nonzero precipitation values (e.g., mixture of gamma and generalized Pareto; Vrac & Naveau, 2007) could also be tested. These efforts are left for future work.

Other large-scale processes besides ENSO are responsible for interannual variability in WR frequency, and future work is needed to better represent these modes of variability in the stochastic simulation process. One extension would be to simply add additional indices that represent other relevant climate modes (e.g., the Pacific Decadal Oscillation), although this would require that scenarios of dynamical change consistently treat changes in ENSO and the PDO or other modes, which are known to be inter-related (Newman et al., 2016). Alternatively, the interannual variability in WRs could be modeled as a latent process, for instance, as a multinomial regression on global approximators (e.g., B-splines and radial basis functions) estimated using the historical WR sequence, that are then simulated using regression and WARM simulations of boundary forcings (e.g., ENSO), but with added noise from the regression model to recover lost variability. These alternatives require further development and testing.

There is also an opportunity to reconstruct and simulate WRs using a network of tree-ring chronologies across North America. There is evidence that large-scale patterns of atmospheric flow are recorded in spatial patterns of wetness in the dendroclimatic record (Wise & Dannenberg, 2014, 2017), and recently, tree rings were used to reconstruct the occurrence of extreme precipitation and ARs associated with WRs 6 and 7 in Figure 2 (Steinschneider et al., 2016, 2018). This underscores the possibility to reconstruct past occurrences of WRs or simulate future sequences (Kwon et al., 2009), based on a wide range of variability presented in the dendroclimatic record, and then to propagate this variability into simulations of local weather. Importantly, the occurrence of only some WRs need to be recorded in indices of tree-ring-based wetness under this strategy, as a change in frequency of some WRs will influence the frequency of others.

Finally, the model was developed specifically for the cold season and only tested in one basin of the western United States. Further work is needed to assess model performance and climate change perturbation strategies in other seasons and regions of the West and also to test whether this model structure is well suited for other regions of the world. For instance, the seasonal distribution of warming is more pronounced at high latitudes [Sejas et al., 2014] and in regions with large differences between winter and summer near-surface water vapor (Cai & Tung, 2012), which can produce locally accelerated warming (Rangwala, 2013). Observational and modeling studies have also suggested that elevation-dependent warming will be most pronounced in the winter (Beniston & Rebetez, 1996; Ceppi et al., 2012; Liu et al., 2009; Rangwala & Miller, 2010) and for minimum daily temperature (Diaz & Bradley, 1997; Hu et al., 2013; Pepin et al., 2015; Rangwala et al., 2016), primarily due to increases in near-surface water vapor from low levels of initial humidity that accelerate the entrapment of long-wave radiation. These characteristics of warming by seasonal and location should be considered in future efforts (e.g., Ray et al., 2018; Schwarz et al., 2018).

7. Conclusion

This study contributes a WR-based stochastic weather generator for climate vulnerability assessments of water systems in the western United States. The hierarchical, semiparametric model uses WRs as a mechanism to bridge between components of the climate system that span a wide range of space and time scales and are relevant to different aspects of the risk profile for water systems. The model is designed to perturb dynamical and thermodynamic features of the climate, enabling a more direct link between emerging hypotheses in climate science and water system vulnerability assessments. In the case study demonstration, the model is shown to effectively reproduce many of the characteristics of climate relevant to water system

performance, while providing options for future climate scenario development that are easy to interpret and communicate. Compared to existing stochastic weather generators designed for vulnerability assessments, the proposed model is designed to frame the range of climate change explored in terms that are consistent with known physical pathways in the climate system. The hope is that such efforts will help bridge the gap between advances in the climate sciences and those at the forefront of water resources systems analysis.

Acknowledgments

The data used in this analysis are publicly available through NOAA online repositories, including the gridded and station-based precipitation and temperature data and NCEP reanalysis. We thank Swen Brands for providing the database of landfalling atmospheric rivers, which is available at <http://www.meteo.unican.es/atmospheric-rivers>. The authors acknowledge support from the U.S. Army Corps of Engineers (IPA000-18-0-0009) and from NSF (grant AGS1702273).

References

- Ailliot, P., Allard, D., Monbet, V., & Naveau, P. (2015). Stochastic weather generators: An overview of weather type models. *Journal Societe Francaise Statistique*, 156, 101–113.
- Allard, D., & Bourotte, M. (2015). Disaggregating daily precipitation into hourly values with a transformed censored latent Gaussian process. *Stochastic Environmental Research and Risk Assessment*, 29(2), 453–462. <https://doi.org/10.1007/s00477-014-0913-4>
- Allen, M. R., & Ingram, W. J. (2002). Constraints on future changes in climate and the hydrologic cycle. *Nature*, 419(6903), 228–232. <https://doi.org/10.1038/nature01092>
- Anderson, T. W., & Goodman, L. A. (1957). Statistical inference about Markov chains. *The Annals of Mathematical Statistics*, 28(1), 89–110. <https://doi.org/10.1214/aoms/1177707039>
- Apipattanas, S., Podestá, G., Rajagopalan, B., & Katz, R. W. (2007). A semiparametric multivariate and multisite weather generator. *Water Resources Research*, 43, W11401. <https://doi.org/10.1029/2006WR005714>
- Bao, J., Sherwood, S. C., Alexander, L. V., & Evans, J. P. (2017). Future increases in extreme precipitation exceed observed scaling rates. *Nature Climate Change*, 7(2), 128–132. <https://doi.org/10.1038/NCLIMATE3201>
- Beniston, M., & Rebetez, M. (1996). Regional behavior of minimum temperatures in Switzerland for the period 1979–1993. *Theoretical and Applied Climatology*, 53(4), 231–243. <https://doi.org/10.1007/BF00871739>
- Boos, W. R. (2012). Thermodynamic scaling of the hydrological cycle of the last glacial maximum. *Journal of Climate*, 25(3), 992–1006. <https://doi.org/10.1175/JCLI-D-11-00010.1>
- Brands, S., Gutiérrez, J. N., & San-Martín, D. (2017). Twentieth-century atmospheric river activity along the west coasts of Europe and North America: algorithm formulation, reanalysis uncertainty and links to atmospheric circulation patterns. *Climate Dynamics*, 48(9–10), 2771–2795. <https://doi.org/10.1007/s00382-016-3095-6>
- Breidl, K., Di Baldassarre, G., Lopez, M. G., Magenlocher, M., Vico, G., & Rutgersson, A. (2017). Can weather generation capture precipitation patterns across different climates, spatial scalars, and under data scarcity. *Nature Scientific Reports*, 7(1), 5449. <https://doi.org/10.1038/s41598-017-05822-y>
- Brekke, L. D., Maurer, E. P., Anderson, J. D., Dettinger, M. D., Townsley, E. S., Harrison, A., & Pruitt, T. (2009). Assessing reservoir operations risk under climate change. *Water Resources Research*, 45, W04411. <https://doi.org/10.1029/2008WR006941>
- Byrne, M. P., & O’Gorman, P. A. (2015). The response of precipitation minus evapotranspiration to climate warming: why the “wet-get-wetter, dry-get-drier” scaling does not hold over land. *Journal of Climate*, 28(20), 8078–8092. <https://doi.org/10.1175/JCLI-D-15-0369.1>
- Cai, M., & Tung, K. (2012). Robustness of dynamical feedbacks from radiative forcing: 2% solar versus 2 x CO₂ experiments in an idealized GCM. *Journal of the Atmospheric Sciences*, 69(7), 2256–2271. <https://doi.org/10.1175/JAS-D-11-0117.1>
- Cai, W., Borlace, S., Lengaigne, M., van Rensch, P., Collins, M., Vecchi, G., et al. (2014). Increasing frequency of extreme El Niño events due to greenhouse warming. *Nature Climate Change*, 4(2), 111–116. <https://doi.org/10.1038/nclimate2100>
- Cai, W., Wang, G., Santoso, A., McPhaden, M. J., Wu, L., Jin, F. F., et al. (2015). Increased frequency of extreme La Niña events under greenhouse warming. *Nature Climate Change*, 5(2), 132–137. <https://doi.org/10.1038/nclimate2492>
- Ceppi, P., Scherrer, S. C., Fischer, A. M., & Appenzeller, C. (2012). Revisiting Swiss temperature trends 1959–2008. *International Journal of Climatology*, 32(2), 203–213. <https://doi.org/10.1002/joc.2260>
- Conticello, F., Cioffi, F., Merz, B., & Lall, U. (2018). An event synchronization method to link heavy rainfall events and large-scale atmospheric circulation features. *International Journal of Climatology*, 38(3), 1421–1437. <https://doi.org/10.1002/joc.5255>
- Dai, A. (2011). Drought under global warming: A review. *WIREs: Climate Change*, 2(1), 45–65.
- Daly, C., Neilson, R. P., & Phillips, D. L. (1994). A statistical topographic model for mapping climatological precipitation over mountainous terrain. *Journal of Applied Meteorology*, 33(2), 140–158. [https://doi.org/10.1175/1520-0450\(1994\)033<0140:ASTMFM>2.0.CO;2](https://doi.org/10.1175/1520-0450(1994)033<0140:ASTMFM>2.0.CO;2)
- Dee, D. P., Uppala, S. M., Simmons, A. J., Berrisford, P., Poli, P., Kobayashi, S., et al. (2011). The ERA-interim reanalysis: Configuration and performance of the data assimilation system. *Quarterly Journal of the Royal Meteorological Society*, 137, 553–597. <https://doi.org/10.1002/qj.828>
- Diaz, H. F., & Bradley, R. S. (1997). Temperature variations during the last century at high elevation sites. *Climate Change*, 36(3–4), 253–279.
- Emori, S., & Brown, S. J. (2005). Dynamic and thermodynamic changes in mean and extreme precipitation under climate change. *Geophysical Research Letters*, 32, L17706. <https://doi.org/10.1029/2005GL023272>
- Evin, G., Favre, A.-C., & Hingray, B. (2018). Stochastic generation of multi-site daily precipitation focusing on extreme events. *Hydrology and Earth System Sciences*, 22(1), 655–672. <https://doi.org/10.5194/hess-22-655-2018>
- Farnham, D. J., Doss-Gollin, J., & Lall, U. (2018). Regional extreme precipitation events: Robust inference from credibly simulated GCM variables. *Water Resources Research*, 54, 3809–3824. <https://doi.org/10.1002/2017WR021318>
- Fischer, E. M., & Knutti, R. (2016). Observed heavy precipitation increase confirms theory and early models. *Nature Climate Change*, 6(11), 986–991. <https://doi.org/10.1038/nclimate3110>
- Fowler, H. J., Blenkinsop, S., & Tebaldi, C. (2007). Review: Linking climate change modeling to impact studies: Recent advances in downscaling techniques for hydrologic modeling. *International Journal of Climatology*, 27(12), 1547–1578. <https://doi.org/10.1002/joc.1556>
- Francis, J. A., & Vavrus, S. J. (2015). Evidence for a wavier jet stream in response to rapid Arctic warming. *Environmental Research Letters*, 10(1). <https://doi.org/10.1088/1748-9326/10/1/014005>
- Guerreiro, S. B., Fowler, H. J., Barbero, R., Westra, S., Lenderink, G., Blenkinsop, S., et al. (2018). Detection of continental-scale intensification of hourly rainfall extremes. *Nature Climate Change*, 8(9), 803–807. <https://doi.org/10.1038/s41558-018-0245-3>
- Guo, D., Westra, S., & Maier, H. R. (2018). An inverse approach to perturb historical rainfall data for scenario-neutral climate impact studies. *Journal of Hydrology*, 556, 877–890. <https://doi.org/10.1016/j.jhydrol.2016.03.025>

- Hawcroft, M., Walsh, E., Hodges, K. I., & Zappa, G. (2018). Significantly increased extreme precipitation expected in Europe and North America from extratropical cyclones. *Environmental Research Letters*, 13(12). <https://doi.org/10.1088/1748-9326/aaed59>
- Held, I. M., & Soden, B. J. (2006). Robust responses of the hydrological cycle to global warming. *Journal of Climate*, 19(21), 5686–5699. <https://doi.org/10.1175/JCLI3990.1>
- Hoell, A., Hoerling, M., Eischeid, J., Wolter, K., Dole, R., Perlwitz, J., et al. (2016). Does El Niño intensity matter for California precipitation? *Geophysical Research Letters*, 43, 819–825. <https://doi.org/10.1002/2015GL067102>
- Hoerling, M. P., Kumar, A., & Xu, T. (2001). Robustness of the nonlinear climate response to ENSO's extreme phases. *Journal of Climate*, 14(6), 1277–1293. [https://doi.org/10.1175/1520-0442\(2001\)014<1277:ROTNCR>2.0.CO;2](https://doi.org/10.1175/1520-0442(2001)014<1277:ROTNCR>2.0.CO;2)
- Holsclaw, T., Greene, A. M., Robertson, A. W., & Smyth, P. (2016). A Bayesian hidden Markov model of daily precipitation over South and East Asia. *Journal of Hydrometeorology*, 17(1), 3–25. <https://doi.org/10.1175/JHM-D-14-0142.1>
- Hu, Y., Maskey, S., & Uhlenbrook, S. (2013). Expected changes in future temperature extremes and their elevation dependency over the Yellow River source region. *Hydrology and Earth System Sciences*, 17(7), 2501–2514. <https://doi.org/10.5194/hess-17-2501-2013>
- Huang, B., Thorne, P. W., Banzon, V. F., Boyer, T., Chepurin, G., Lawrimore, J. H., et al. (2017). Extended reconstructed sea surface temperature, version 5 (ERSSTv5): upgrades, validations, and intercomparisons. *Journal of Climate*, 30(20), 8179–8205. <https://doi.org/10.1175/JCLI-D-16-0836.1>
- Hughes, J. P., & Guttorp, P. (1994). A class of stochastic models for relating synoptic atmospheric patterns to regional hydrologic phenomena. *Water Resources Research*, 30(5), 1535–1546. <https://doi.org/10.1029/93WR02983>
- Jiménez Cisneros, B. E., Oki, T., Arnell, N. W., Benito, G., Cogley, J. G., Döll, P., et al. (2014). Freshwater resources. In C. B. Field, V. R. Barros, D. J. Dokken, K. J. Mach, M. D. Mastrandrea, T. E. Bilir, M. Chatterjee, K. L. Ebi, Y. O. Estrada, R. C. Genova, B. Girma, E. S. Kissel, A. N. Levy, S. MacCracken, P. R. Mastrandrea, & L. L. White (Eds.), *Climate change 2014: Impacts, adaptation, and vulnerability. Part A: Global and sectoral aspects. Contribution of Working Group II to the Fifth Assessment Report of the Intergovernmental Panel on Climate Change*, (pp. 229–269). Cambridge, United Kingdom and New York, NY, USA: Cambridge University Press.
- Johnson, F., & Sharma, A. (2009). Measurement of GCM skill in predicting variables relevant for hydroclimatological assessments. *Journal of Climate*, 22(16), 4373–4382. <https://doi.org/10.1175/2009JCLI2681.1>
- Käärik, M., Selart, A., Käärik, E., & Liivi, J. (2011). The use of copulas to model conditional expectation for multivariate data, in ISI Proc. 58th World Statistical Congress, 5533–5538.
- Kanamitsu, M., Ebisuzaki, W., Woollen, J., Yang, S.-K., Hnilo, J. J., Fiorino, M., & Potter, G. L. (2002). NCEP-DOE AMIP-II Reanalysis (R-2). *Bulletin of the American Meteorological Society*, 83(11), 1631–1643. [https://doi.org/10.1175/bams-83-11-1631\(2002\)083<1631:nar>2.3.co;2](https://doi.org/10.1175/bams-83-11-1631(2002)083<1631:nar>2.3.co;2)
- Kendon, E. J., Ban, N., Roberts, N. M., Fowler, H. J., Roberts, M. J., Chan, S. C., et al. (2017). Do convection-permitting regional climate models improve projections of future precipitation change? *Bulletin of the American Meteorological Society*, 98(1), 79–93. <https://doi.org/10.1175/BAMS-D-15-0004.1>
- Knighton, J., Steinschneider, S., & Walter, M. T. (2017). A vulnerability-based, bottom-up assessment of future riverine flood risk using a modified peaks-over-threshold approach and a physically based hydrologic model. *Water Resources Research*, 53, 10043–10064. <https://doi.org/10.1002/2017WR021036>
- Kwon, H.-H., Lall, U., & Khalil, A. F. (2007). Stochastic simulation model for nonstationary time series using an autoregressive wavelet decomposition: Applications to rainfall and temperature. *Water Resources Research*, 43, W05407. <https://doi.org/10.1029/2006WR005258>
- Kwon, H.-H., Lall, U., & Obeysekera, J. (2009). Simulation of daily rainfall scenarios with interannual and multidecadal climate cycles for South Florida. *Stochastic Environmental Research and Risk Assessment*, 23(7), 879–896. <https://doi.org/10.1007/s00477-008-0270-2>
- Kysely, J., Rulfova, Z., Farda, A., & Hanel, M. (2015). Convective and stratiform precipitation characteristics in an ensemble of regional climate model simulations. *Climate Dynamics*, 46(1-2), 227–243. <https://doi.org/10.1007/s00382-015-2580-7>
- Lenderink, G., Barbero, R., Loriaux, J. M., & Fowler, H. J. (2017). Super-Clausius–Clapeyron scaling of extreme hourly convective precipitation and its relation to large-scale atmospheric conditions. *Journal of Climate*, 30(15), 6037–6052. <https://doi.org/10.1175/JCLI-D-16-0808.1>
- Li, G., Harrison, S. P., Bartlein, P. J., Izumi, K., & Colin Prentice, I. (2013). Precipitation scaling with temperature in warm and cold climates: An analysis of CMIP5 simulations. *Geophysical Research Letters*, 40, 4018–4024. <https://doi.org/10.1002/grl.50730>
- Li, W., Li, L., Ting, M., & Liu, Y. (2012). Intensification of Northern Hemisphere subtropical highs in a warming climate. *Nature Geoscience*, 5(11), 830–834. <https://doi.org/10.1038/NCEO01590>
- Li, X., & Babovic, V. (2018). A new scheme for multivariate, multisite weather generator with inter-variable, inter-site dependence and inter-annual variability based on empirical copula approach. *Climate Dynamics*, 52(3-4), 2247–2267. <https://doi.org/10.1007/s00382-018-4249-5A>
- Liu, X., Cheng, Z., Yan, L., & Yin, Z. (2009). Elevation dependency of recent and future minimum surface air temperature trends in the Tibetan Plateau and its surroundings. *Global and Planetary Change*, 68(3), 164–174. <https://doi.org/10.1016/j.gloplacha.2009.03.017>
- Livneh B., Bohn, T. J., Pierce, D. S., Munoz-Ariola, F., Nijssen, B., Vose, R., et al. (2015). A spatially comprehensive, hydrometeorological data set for Mexico, the U.S., and southern Canada 1950–2013, Nature Scientific Data, 5:150042, doi:10.1038/sdata.2015.42.
- Lu, J., Ruby Leung, L., Yang, Q., Chen, G., Collins, W. D., Li, F., et al. (2014). The robust dynamical contribution to precipitation extremes in idealized warming simulations across model resolutions. *Geophysical Research Letters*, 41, 2971–2978. <https://doi.org/10.1002/2014GL059532>
- Maher, P., Vallis, G. K., Sherwood, S. C., Webb, M. J., & Sansom, P. G. (2018). The impact of parameterized convection on climatological precipitation in atmospheric global climate models. *Geophysical Research Letters*, 45, 3728–3736. <https://doi.org/10.1002/2017GL076826>
- Mallet, P.-E., Claud, C., & Vicomte, M. (2017). North Atlantic polar lows and weather regimes: do current links persist in a warmer climate? *Atmospheric Science Letters*, 18(8), 349–355. <https://doi.org/10.1002/asl.763>
- Milrad, S. (2018). *Synoptic analysis and forecasting*, (p. 246). Elsevier. <https://doi.org/10.1016/C2015-0-05604-0>
- Muller, C. J., & O'Gorman, P. A. (2011). An energetic perspective on the regional response of precipitation to climate change. *Nature Climate Change*, 1(5), 266–271. <https://doi.org/10.1038/nclimate1169>
- Muñoz, Á. G., Yang, X., Vecchi, G. A., Robertson, A. W., & Cooke, W. F. (2017). A weather-type-based cross-time-scale diagnostic framework for coupled circulation models. *Journal of Climate*, 30(22), 8951–8972. <https://doi.org/10.1175/JCLI-D-17-0115.1>
- Newman, M., Alexander, M. A., Ault, T. R., Cobb, K. M., Deser, C., di Lorenzo, E., et al. (2016). The Pacific Decadal Oscillation, Revisited. *Journal of Climate*, 29(12), 4399–4427. <https://doi.org/10.1175/JCLI-D-15-0508.1>

- Nowak, K. C., Rajagopalan, B., & Zagana, E. (2011). Wavelet auto-regressive method (WARM) for multi-site streamflow simulation of data with non-stationary spectra. *Journal of Hydrology*, 410(1-2), 1–12. <https://doi.org/10.1016/j.jhydrol.2011.08.051>
- O’Gorman, P. A. (2015). Precipitation extremes under climate change. *Current Climate Change Reports*, 1(2), 49–59. <https://doi.org/10.1007/s40641-015-0009-3>
- Pendergrass, A. G., & Hartmann, D. L. (2014a). The atmospheric energy constraint on global-mean precipitation change. *Journal of Climate*, 27(2), 757–768. <https://doi.org/10.1175/JCLI-D-13-00163.1>
- Pendergrass, A. G., & Hartmann, D. L. (2014b). Two modes of change of the distribution of rain. *Journal of Climate*, 27(22), 8357–8371. <https://doi.org/10.1175/JCLI-D-14-00182.1>
- Pepin, N., Bradley, R. S., Diaz, H. F., Baraer, M., Caceres, E. B., Forsythe, N., et al. (2015). Elevation-dependent warming in mountain regions of the world. *Nature Climate Change*, 5(5), 424–430. <https://doi.org/10.1038/nclimate2563>
- Pepin, N. C., & Lundquist, J. D. (2008). Temperature trends at high elevations: Patterns across the globe. *Geophysical Research Letters*, 35, L14701. <https://doi.org/10.1029/2008GL034026>
- Pfahl, S., O’Gorman, P. A., & Fischer, E. M. (2017). Understanding the regional pattern of projected future changes in extreme precipitation. *Nature Climate Change*, 7(6), 423–427. <https://doi.org/10.1038/nclimate3287>
- Quinn, J. D., Reed, P. M., Giuliani, M., Castelletti, A., Oyler, J. W., & Nicholas, R. E. (2018). Exploring how changing monsoonal dynamics and human pressures challenge multireservoir management for flood protection, hydropower production, and agricultural water supply. *Water Resources Research*, 54, 4638–4662. <https://doi.org/10.1029/2018WR022743>
- Rangwala, I. (2013). Amplified water vapour feedback at high altitudes during winter. *International Journal of Climatology*, 33(4), 897–903. <https://doi.org/10.1002/joc.3477>
- Rangwala, I., & Miller, J. R. (2010). Twentieth century temperature trends in Colorado’s San Juan Mountains. *Arctic Antarctic and Alpine Research*, 42(1), 89–97. <https://doi.org/10.1657/1938-4246-42.1.89>
- Rangwala, I., & Miller, J. R. (2012). Climate change in mountains: A review of elevation-dependent warming and its possible causes. *Climate Change*, 114(3-4), 527–547. <https://doi.org/10.1007/s10584-012-0419-3>
- Rangwala, I., Sinsky, E., & Miller, J. R. (2016). Variability in projected elevation dependent warming in boreal midlatitude winter in CMIP5 climate models and its potential drivers. *Climate Dynamics*, 46(7-8), 2115–2122. <https://doi.org/10.1007/s00382-015-2692-0>
- Ray, P. A., Bonzanigo, L., Wi, S., Yang, Y. E., Karki, P., Garcia, L., et al. (2018). Multidimensional stress test for hydropower investments facing climate, geophysical and financial uncertainty. *Global Environmental Change*, 48, 168–181. <https://doi.org/10.1016/j.gloenvcha.2017.11.013>
- Richardson, C. W. (1981). Stochastic simulation of daily precipitation, temperature, and solar radiation. *Water Resources Research*, 17(1), 182–190. <https://doi.org/10.1029/WR017i001p00182>
- Rivera, E. R., Dominguez, F., & Castro, C. L. (2014). Atmospheric rivers and cool season extreme precipitation events in the Verde River Basin of Arizona. *Journal of Hydrometeorology*, 15(2), 813–829. <https://doi.org/10.1175/JHM-D-12-0189.1>
- Robertson, A. W., & Ghil, M. (1999). Large-scale weather regimes and local climate over the western United States. *Journal of Climate*, 12(6), 1796–1813. [https://doi.org/10.1175/1520-0442\(1999\)012<1796:LSWRAL>2.0.CO;2](https://doi.org/10.1175/1520-0442(1999)012<1796:LSWRAL>2.0.CO;2)
- Robertson, A. W., Kirshner, S., & Smyth, P. (2004). Downscaling of daily rainfall occurrence over northeast Brazil using a hidden Markov model. *Journal of Climate*, 17(22), 4407–4424. <https://doi.org/10.1175/JCLI-3216.1>
- Robertson, A. W., Kushnir, Y., Lall, U., & Nakamura, J. (2015). *Weather and climatic drivers of extreme flooding events over the Midwest of the United States. Extreme Events: Observations, Modeling, and Economics*, Geophys.Monogr, American Geophysical Union, (Vol. 214, pp. 113–124).
- Schwarz, A., P. Ray, S. Wi, C. Brown, M. He, and M. Correa (2018), Climate change risks faced by the California Central Valley water resource system, in California’s Fourth Climate Assessment, State of California, Sacramento, California.
- Seager, R., Hoerling, M., Schubert, S., Wang, H., Lyon, B., Kumar, A., et al. (2015). Causes of the 2011–14 California drought. *Journal of Climate*, 28(18), 6997–7024. <https://doi.org/10.1175/JCLI-D-14-00860.1>
- Seager, R., Naik, N., & Vecchi, G. A. (2010). Thermodynamic and dynamic mechanisms for large-scale changes in the hydrologic cycle in response to global warming. *Journal of Climate*, 23(17), 4651–4668. <https://doi.org/10.1175/2010JCLI3655.1>
- Seager, R., Neelin, D., Simpson, I., Liu, H., Henderson, N., Shaw, T., et al. (2014). Dynamical and thermodynamical causes of large-scale changes in the hydrological cycle over North America in response to global Warming. *Journal of Climate*, 27(20), 7921–7948. <https://doi.org/10.1175/JCLI-D-14-00153.1>
- Seager, R., & Vecchi, G. A. (2010). Greenhouse warming and the 21st century hydroclimate of southwestern North America. *PNAS*, 107(50), 21277–21282. <https://doi.org/10.1073/pnas.0910856107>
- Sejas, S. A., Cai, M., Hu, A., Meehl, G. A., Washington, W., & Taylor, P. C. (2014). Individual feedback contributions to the seasonality of surface warming. *Journal of Climate*, 27(14), 5653–5669. <https://doi.org/10.1175/JCLI-D-13-00658.1>
- Shepard, D. S. (1984). Computer mapping. In G. L. Gaile, C. J. Willmott, & D. Reidel (Eds.), *The SYMAP interpolation algorithm, Spatial Statistics and Models*, (pp. 133–145). Dordrecht: Springer.
- Shepherd, T. G. (2014). Atmospheric circulation as a source of uncertainty in climate change projections. *Nature Geosciences*, 7(10), 703–708. <https://doi.org/10.1038/ngeo2253>
- Singh, R., Wagener, T., Crane, R., Mann, M. E., & Ning, L. (2014). A vulnerability driven approach to identify adverse climate and land use change combinations for critical hydrologic indicator thresholds: Application to a watershed in Pennsylvania, USA. *Water Resources Research*, 50, 3409–3427. <https://doi.org/10.1002/2013WR014988>
- Sparks, N. J., Hardwick, S. R., Schmid, M., & Toumi, R. (2018). IMAGE: A multivariate multi-site stochastic weather generator for European weather and climate. *Stochastic Environmental Research and Risk Assessment*, 32(3), 771–784. <https://doi.org/10.1007/s00477-017-1433-9>
- Steinschneider, S., & Brown, C. (2013). A semiparametric multivariate, multi-site weather generator with low-frequency variability for use in climate risk assessments. *Water Resources Research*, 49, 7205–7220. <https://doi.org/10.1002/wrcr.20528>
- Steinschneider, S., Ho, M., Cook, E. R., & Lall, U. (2016). Can PDSI inform extreme precipitation?: An exploration with a 500 year long paleoclimate reconstruction over the U.S. *Water Resources Research*, 52, 3866–3880. <https://doi.org/10.1002/2016WR018712>
- Steinschneider, S., Ho, M., Williams, A. P., Cook, E. R., & Lall, U. (2018). A 500-year tree ring-based reconstruction of extreme cold-season precipitation and number of atmospheric river landfalls across the southwestern United States. *Geophysical Research Letters*, 45(11), 5672–5680. <https://doi.org/10.1029/2018GL078089>
- Steinschneider, S., McCrary, R., Mearns, L. O., & Brown, C. (2015). The effects of climate model similarity on probabilistic climate projections and the implications for local, risk-based adaptation planning. *Geophysical Research Letters*, 42, 5014–5044. <https://doi.org/10.1002/2015GL064529>

- Steinschneider, S., McCrary, R., Wi, S., Mulligan, K., Mearns, L., & Brown, C. (2015). Expanded decision-scaling framework to select robust long-term water-system plans under hydroclimatic uncertainties. *Journal of Water Resources Planning and Management*, 141(11). [https://doi.org/10.1061/\(ASCE\)WR.1943-5452.0000536](https://doi.org/10.1061/(ASCE)WR.1943-5452.0000536)
- Steinschneider, S., Wi, S., & Brown, C. (2015). The integrated effects of climate and hydrologic uncertainty on future flood risk assessments. *Hydrological Processes*, 29(12), 2823–2839. <https://doi.org/10.1002/hyp.10409>
- Stephens, G. L., L'Ecuier, T., Forbes, R., Gettleman, A., Golaz, J.-C., Bodas-Salcedo, A., et al. (2010). Dreary state of precipitation in global models. *Journal of Geophysical Research*, 115, D24211. <https://doi.org/10.1029/2010JD014532>
- Stephenson, D. B., Collins, M., Rougier, J. C., & Chandler, R. E. (2012). Statistical problems in the probabilistic prediction of climate change. *Environmetrics*, 23(5), 364–372. <https://doi.org/10.1002/env.2153>
- Tan, J., Oreopoulos, L., Jakob, C., & Jin, D. (2018). Evaluating rainfall errors in global climate models through cloud regimes. *Climate Dynamics*, 50(9–10), 3301–3314. <https://doi.org/10.1007/s00382-017-3806-7>
- Taylor, K. E., Stouffer, R. J., & Meehl, G. A. (2012). An overview of CMIP5 and the experiment design. *Bulletin of the American Meteorological Society*, 93(4), 485–498. <https://doi.org/10.1175/BAMS-D-11-00094.1>
- Ting, M., Seager, R., Li, C., Liu, H., & Henderson, N. (2018). Mechanism of future spring drying in the southwestern United States in CMIP5 models. *Journal of Climate*, 31(11), 4265–4279. <https://doi.org/10.1175/JCLI-D-17-0574.1>
- Trenberth, K. E. (2011). Changes in precipitation with climate change. *Climate Research*, 47(1), 123–138. <https://doi.org/10.3354/cr00953>
- Trenberth, K. E., Dai, A., van der Schrier, G., Jones, P. D., Barichivich, J., Briffa, K. R., & Sheffield, J. (2014). Global warming and changes in drought. *Nature Climate Change*, 4(1), 17–22. <https://doi.org/10.1038/NCLIMATE2067>
- Verdin, A., Rajagopalan, B., Kleiber, W., Podestá, G., & Bert, F. (2018). A conditional stochastic weather generator for seasonal to multi-decadal simulations. *Journal of Hydrology*, 556, 835–846. <https://doi.org/10.1016/j.jhydrol.2015.12.036>
- Vrac, M., & Naveau, P. (2007). Stochastic downscaling of precipitation: From dry events to heavy rainfalls. *Water Resources Research*, 43, W07402. <https://doi.org/10.1029/2006WR005308>
- Westra, S., Fowler, H. J., Evans, J. P., Alexander, L. V., Berg, P., Johnson, F., et al. (2014). Future changes to the intensity and frequency of short- duration extreme rainfall. *Reviews of Geophysics*, 52, 522–555. <https://doi.org/10.1002/2014RG000464>
- Wilks, D. S. (2002). Realizations of daily weather in forecast seasonal climate. *Journal of Hydrometeorology*, 3(2), 195–207. [https://doi.org/10.1175/1525-7541\(2002\)003<0195:RODWIF>2.0.CO;2](https://doi.org/10.1175/1525-7541(2002)003<0195:RODWIF>2.0.CO;2)
- Wilks, D. S. (2010). Use of stochastic weather generators for precipitation downscaling. *WIREs Clim Change*, 1(6), 898–907. <https://doi.org/10.1002/wcc.85>
- Wilks, D. S. (2012). Stochastic weather generators for climate-change downscaling. Part II: Multivariate and spatially coherent multisite downscaling. *WIREs: Climate Change*, 3(3), 267–278.
- Wilks, D. S., & Wilby, R. L. (1999). The weather generation game: A review of stochastic weather models. *Progress in Physical Geography*, 23(3), 329–357. <https://doi.org/10.1177/030913339902300302>
- Wise, E. K., & Dannenberg, M. P. (2014). Persistence of pressure patterns over North America and the North Pacific since AD 1500. *Nature Communications*, 5(1), 4912. <https://doi.org/10.1038/ncomms5912>
- Wise, E. K., & Dannenberg, M. P. (2017). Reconstructed storm tracks reveal three centuries of changing moisture delivery to North America. *Science Advances*, 3(6), e1602263. <https://doi.org/10.1126/sciadv.1602263>
- Yates, D. N., Miller, K. A., Wilby, R. L., & Kaatz, L. (2015). Decision-centric adaptation appraisal for water management across Colorado's Continental Divide. *Climate Risk Management*, 10, 35–50. <https://doi.org/10.1016/j.crm.2015.06.001>
- Yeh, S.-W., Cai, W., Min, S.-K., McPhaden, M. J., Dommenges, D., Dewitte, B., & Kug, J.-S. (2018). ENSO atmospheric teleconnections and their response to greenhouse gas forcing. *Reviews of Geophysics*, 56, 185–206. <https://doi.org/10.1002/2017RG000568>